Biogeosciences Discuss., 10, 13931–13976, 2013
www.biogeosciences-discuss.net/10/13931/2013/
doi:10.5194/bgd-10-13931-2013

Biogeosciences Discussions
Open Access

Top-down, bottom-up and physical controls on diatom-diazotroph assemblage growth in the Amazon River Plume

M. R. Stukel, V. J. Coles, M. T. Brooks, and R. R. Hood

University of Maryland Center for Environmental Science, Horn Point Laboratory, 21613 Cambridge, Maryland, USA

Received: 3 August 2013 – Accepted: 15 August 2013 – Published: 23 August 2013

Correspondence to: M. R. Stukel (mstukel@umces.edu)

Published by Copernicus Publications on behalf of the European Geosciences Union.

Abstract

The nutrient-rich waters of the Amazon River Plume (ARP) support dense blooms of diatom-diazotroph assemblages (DDA) that introduce large quantities of new nitrogen to the planktonic ecosystem and, unlike other nitrogen-fixers, are likely to directly fuel vertical carbon flux. To investigate the factors controlling DDA blooms, we develop a five phytoplankton (cyanobacteria, diatoms, unicellular microbial diazotrophs, DDA, and *Trichodesmium*), two zooplankton model and embed it within a 1/6° resolution physical model of the tropical and subtropical Atlantic. The model generates realistic DDA blooms in the ARP and also exhibits basin-wide primary production, nitrogen fixation, and grazing rates consistent with observed values. By following ARP water parcels with synthetic Lagrangian drifters released at the river mouth we are able to assess the relative impacts of grazing, nutrient supply, and physical forcing on DDA bloom formation. DDA bloom formation is stimulated in the silica-rich water of the ARP by decreases in grazing pressure when mesozooplankton (which co-occur in high densities with coastal diatom blooms) concentrations decrease. Bloom termination is driven primarily by silica limitation of the DDA. In agreement with in situ data, this net growth niche for DDA exists in a salinity range from ~ 20–34 PSU, although this co-occurrence is coincidental rather than causative. Because net growth rates are relatively modest, bloom formation in ARP water parcels depends critically on the time spent in this ideal habitat, with high DDA biomass only occurring when water parcels spent > 23 days in the optimal habitat niche.

1 Introduction

The Amazon River discharges $1.93 \times 10^5\ m^3\ s^{-1}$ (Perry et al., 1996) of nutrient-rich freshwater into the Western Tropical North Atlantic (WTNA). This low-salinity water forms a surface plume of up to $1.2 \times 10^6\ km^2$ that can extend greater than 3000 km from the river mouth (Hu et al., 2004) and supports a successional series of phytoplankton

BGD
10, 13931–13976, 2013

communities within the gradient from rich coastal waters to oligotrophic offshore regions where the plume dissipates into the tropical and subtropical Atlantic. Subramaniam et al. (2008) defined three regions within the plume (oligohaline, mesohaline, and oceanic) each supporting distinct phytoplankton assemblages. The eutrophic oligohaline region supported a community of coastal diatom species concentrated near the surface due to the low light transmission within the plume. The coastal diatoms transitioned to diatom-diazotroph assemblages (DDA) in the mesohaline waters, presumably due to nitrate depletion, leading to high N_2-fixation (Nfix) and carbon export rates. Offshore, in the oceanic regions, the DDA were replaced by a typical oceanic phytoplankton distribution with *Trichodesmium* dominating the N_2-fixing assemblage and significantly reduced Nfix rates. Subramaniam et al. (2008) attribute this successional cycle to a series of bottom-up controls of the phytoplankton community.

While this bottom-up, or nutrient supply, control mechanism is plausible and consistent with in situ patterns, it does not explain the dominance of DDA over unicellular microbial diazotrophs (UMD) in the plume. An alternative hypothesis would state that top-down, or grazing, control of UMD by protozoa offers DDA a competitive advantage in the low-nitrogen mesohaline waters and DDA lose to the relatively grazer-resistant *Trichodesmium* after mesozooplankton grazing pressure on DDA increases.

Regardless of the ecological mechanisms promoting their growth, Nfix by DDA (rather than UMD and *Trichodesmium*) in the plume may lead to vastly different fates for the nitrogen and carbon they fix. Unlike *Trichodesmium* and typical UMD (such as *Crocosphaera*), siliceous DDA are significantly denser than water and hence likely to sink out of the euphotic zone, either as individual cells, aggregates, or after grazing and packaging into fecal pellets. Their presence thus may catalyze the export of carbon to deeper depths. The mesohaline region characterized by DDA blooms has been found to have higher rates of carbon export and DIC drawdown (Cooley and Yager, 2006; Subramaniam et al., 2008). Despite this potentially important and unique biogeochemical role for DDA, biogeochemical models that incorporate diazotrophy have primarily focused solely on *Trichodesmium* (Coles and Hood, 2007; Hood et al., 2004;

BGD
10, 13931–13976, 2013

Moore et al., 2006; Yoshikawa et al., 2013). An interesting exception to this pattern was made by Monteiro et al. (2010), who studied the competition between 78 species of randomly generated phytoplankton including three classes of diazotrophs representing *Trichodesmium*, DDA, and UMD. The authors noted, however, that their model did not represent DDA as accurately as *Trichodesmium* and UMD.

To investigate both the control mechanisms of ecological succession and its biogeochemical effects in the Amazon River Plume (ARP) and WTNA we embedded a 5 phytoplankton model within a detailed three dimensional physical model of the tropical and subtropical Atlantic (Coles et al., 2013). We compare model mean rates to measurements made throughout the North Atlantic, but also focus specifically on the model's ability to replicate the DDA-salinity relationships in the ARP found by Subramaniam et al. (2008). A key feature of our work is the use of synthetic Lagrangian drifters, which allow us to track parcels of river water as they enter the WTNA and simultaneously determine DDA concentrations and growth and loss rates. We show that DDA bloom dynamics are driven by the interplay of top-down and bottom-up forcing with physically driven dilution with oligotrophic water.

2 Methods

2.1 Numerical and physical framework

The biological model (explained below) was implemented within a 1/6° Hybrid Coordinate Ocean Model (HYCOM) physical framework extending from 15° S to 40° N. Surface forcing from the European Centre for Medium-Range Weather Forecasts reanalysis (ERA40) at 6 hourly intervals and climatological mean river inputs were used to force the model (Coles et al., 2013). The physical model was spun up for 20 yr before the ecological model was introduced. Nutrient fields were initialized (and relaxed near the model boundaries) according to the Polar Science Center Hydrographic Climatology (Steele et al., 2001). The ecological model was implemented using a positive

BGD
10, 13931–13976, 2013

definite backward-Euler numerical scheme and spun up for 20 yr (1979–1998), then run again from 1979–1998. 25 synthetic Lagrangian surface drifters (Halliwell and Garraffo, 2002) were released in the model in a 500 km by 150 km band near the river mouth on the continental shelf every five days and tracked for a period of 400 days (or until the float ran aground).

Because growth kinetics of the mixed communities of ARP phytoplankton taxa modeled in this study have not yet been determined, we do not try to constrain our model using specifically measured in situ or laboratory values. Rather, we started with initial parameter values derived primarily from the Coles et al. (2007) *Trichodesmium* and PISCES (Aumont et al., 2003) models and then tuned the parameters within what we considered biologically realistic ranges until model behavior approximated the ARP ecosystem (Table A1).

2.2 Ecological model construction

Our model contains three nutrients (N, P, and Si), five phytoplankton (cyanobacteria – P_{Cya}, unicellular microbial diazotrophs – P_{UMD}, diatoms – P_{Dtm}, diatom-diazotroph assemblages – P_{DDA}, and *Trichodesmium* – P_{Tri}), and two zooplankton (protozoans – Z_S and mesozooplankton – Z_L). It also contains three detrital compartments: dissolved and colloidal organic matter (D_C), small detritus (D_S), and large detritus (D_L). While all living compartments are assumed to have fixed elemental stoichiometries, detrital pools have variable stoichiometry (Fig. 1).

Our five phytoplankton communities include two pairs of diazotroph-non-diazoatroph analogs (UMD and Cya; DDA and Dtm). In the absence of evidence, we have taken the Occam's razor approach and assume that our analog pairs behave identically with respect to grazing, light absorption, and nutrient kinetics. Our diazotroph-non-diazotroph analogs thus differ only in their maximum growth rates (and of course the non-diazotroph's nitrogen requirement). Cyanobacterial growth is given below, with α as the phytoplankton growth efficiency ($1 - \alpha$, is the fraction lost to DOC) and m_P the

BGD
10, 13931–13976, 2013

phytoplankton mortality/respiration rate (for parameter values, see Table A1).

$$\frac{dP_{Cya}}{dt} = \alpha \cdot U_{Cya} \cdot P_{Cya} - m_{PS} \cdot P_{Cya} - G_{S,Cya} \cdot Z_S \quad (1)$$

$G_{S,Cya}$ is the grazing rate of protozoan zooplankton (Z_S) on cyanobacteria (explained in more detail below). U_{Cya} is the cyanobacterial nutrient uptake rate and is a function of light (with photoinhibition near the surface), maximum growth rate (μ_{small}), and nutrients. Nutrient limitation is modeled as a monod-type response to limitation by either dissolved inorganic nitrogen (N) or dissolved inorganic phosphorus (DIP).

$$U_{Cya}(N,DIP,I) = \mu_{small} \cdot e^{-I/I_{\beta PS}} \cdot \left(1 - e^{-I/I_{PS}}\right) \cdot \min\left(\frac{N}{K_{S,N}+N}, \frac{DIP}{K_{S,P}+DIP}\right) \quad (2)$$

UMD growth is modeled similarly to cyanobacterial growth, though we assume that nitrogen is no longer limiting, diazotrophs have a higher N : P ratio than normal phytoplankton, and that nitrogen-fixers have a lower maximum growth rate ($\mu_{small} \times \vartheta_S$) due to the increased energetic cost of fixing N_2, relative to utilizing NO_3 or NH_4^+.

$$\frac{dP_{UMD}}{dt} = \alpha \cdot V_{UMD} \cdot P_{UMD} - m_{PS} \cdot P_{UMD} - G_{S,UMD} \cdot Z_S \quad (3)$$

$$V_{UMD}(DIP,I) = \mu_{small} \cdot \vartheta_S \cdot e^{-I/I_{\beta PS}} \cdot \left(1 - e^{-I/I_{PS}}\right) \cdot \frac{DIP}{K_{S,P}+DIP} \quad (4)$$

Diatom growth is assumed to proceed with a higher maximum growth rate (μ_{large}) and a Si requirement. Diatoms have an additional loss term associated with mesozooplankton grazing (explained below).

$$\frac{dP_{Dtm}}{dt} = \alpha \cdot U_{Dtm} \cdot P_{Dtm} - m_{PL} \cdot P_{Dtm} - G_{S,Dia} \cdot Z_S - G_{L,Dia} \cdot Z_L \quad (5)$$

$$U_{Dtm}(N,DIP,Si,I) = \mu_{large} \cdot e^{-I/I_{\beta PL}} \cdot \left(1 - e^{-I/I_{PL}}\right) \cdot \min\left(\frac{N}{K_{L,N}+N}, \frac{DIP}{K_{L,P}+DIP}, \frac{Si}{K_{Si}+Si}\right) \quad (6)$$

BGD
10, 13931–13976, 2013

DDA are assumed to behave similarly to other diatoms when DIN is relatively more abundant than Si or DIP, though with a slightly reduced maximum growth rate ($\mu_{\text{large}} \times \vartheta_{\text{L}}$). When DIN is limiting, DDA continue to grow, but at a much reduced maximum growth rate ($\mu_{\text{large}} \times \vartheta_{\text{Nif}}$), such that DDA rates of change are governed by the equations:

$$\frac{dP_{\text{DDA}}}{dt} = \alpha \cdot U_{\text{DDA}} \cdot P_{\text{Dtm}} - m_{\text{PL}} \cdot P_{\text{DDA}} - G_{\text{S,DDA}} \cdot Z_{\text{S}} - G_{\text{L,DDA}} \cdot Z_{\text{L}} \quad (7)$$

$$U_{\text{DDA}}(\text{N,DIP,Si},I) = \mu_{\text{large}} \cdot \vartheta_{\text{L}} \cdot e^{-I/I_{\beta\text{PL}}} \cdot \left(1 - e^{-\frac{I}{I_{\text{PL}}}}\right) \cdot \min\left(\frac{\text{N}}{K_{\text{L,N}} + \text{N}}, \frac{\text{DIP}}{K_{\text{L,P}} + \text{DIP}}, \frac{\text{Si}}{K_{\text{Si}} + \text{Si}}\right)$$
$$+ \mu_{\text{large}} \cdot \vartheta_{\text{nif}} \cdot e^{-I/I_{\beta\text{PL}}} \cdot \left(1 - e^{-\frac{I}{I_{\text{PL}}}}\right) \cdot \left(\min\left(\frac{\text{DIP}}{K_{\text{L,P}} + \text{DIP}}, \frac{\text{Si}}{K_{\text{Si}} + \text{Si}}\right)\right.$$
$$\left. - \min\left(\frac{\text{N}}{K_{\text{L,N}} + \text{N}}, \frac{\text{DIP}}{K_{\text{L,P}} + \text{DIP}}, \frac{\text{Si}}{K_{\text{Si}} + \text{Si}}\right)\right) \quad (8)$$

thus when nitrogen is not limiting, the U_{DDA} reduces to $\theta_{\text{L}} \times F(\text{DIP,Si},I)$ and in the limit as N, U_{DDA} reduces to $\theta_{\text{L}} \times F(\text{DIP,Si},I)$, where:

$$F(\text{DIP,Si},I) = \mu_{\text{large}} \cdot e^{-I/I_{\beta\text{PL}}} \cdot \left(1 - e^{-\frac{I}{I_{\text{PL}}}}\right) \cdot \min\left(\frac{\text{DIP}}{K_{\text{L,P}} + \text{DIP}}, \frac{\text{Si}}{K_{\text{Si}} + \text{Si}}\right) \quad (9)$$

As in Hood et al. (2001), *Trichodesmium* is parameterized with a lower growth rate (μ_{Tri}) than the other phytoplankton, but without photoinhibition. Both protozoan and metazoan zooplankton are assumed capable of ingesting *Trichodesmium*, though both grazers are assumed to preferentially graze smaller phytoplankton rather than *Trichodesmium*.

$$\frac{dP_{\text{Tri}}}{dt} = \alpha \cdot V_{\text{Tri}}(\text{DIP},I) \cdot P_{\text{Tri}} - m_{\text{PT}} \cdot P_{\text{Tri}} - G_{\text{S,Tri}} \cdot Z_{\text{S}} - G_{\text{L,Tri}} \cdot Z_{\text{L}}$$
$$V_{\text{Tri}}(\text{DIP},I) = \mu_{\text{Tri}} \cdot \left(1 - e^{-I/I_{\text{PT}}}\right) \cdot \frac{\text{DIP}}{K_{\text{T,P}} + \text{DIP}} \quad (10)$$

BGD
10, 13931–13976, 2013

Protozoan zooplankton (Z_S) are assigned a growth gross efficiency of γ_S. They are assumed to be capable of consuming each phytoplankton group with a maximum grazing rate on the total community of G_{S0}. We assume preferential grazing on smaller phytoplankton such that if all phytoplankton size classes were equally abundant (with respect to biomass), G_{SS} (Cyanobacteria) > G_{SL} (Diatoms) > G_{ST} (*Trichodesmium*). We also assume that grazers can not differentiate between nitrogen-fixing and non-nitrogen-fixing phytoplankton of the same size. Phytoplankton abundances with respect to grazing preferences are assigned based on nitrogen biomasses. Protozoans are lost to grazing by mesozooplankton as well as a linear mortality term.

$$\frac{dZ_S}{dt} = \gamma_S \cdot \mathrm{GTS} \cdot Z_S - m_{ZS} \cdot Z_S - G_{LZ} \cdot Z_L \tag{11}$$

Total Protozoan grazing is:

$$\mathrm{GTS} = G_{S,Cya} + G_{S,UMD} \cdot \frac{R_0}{R_n} + G_{S,Dtm} + G_{S,DDA} \cdot \frac{R_0}{R_n} + G_{S,Tri} \cdot \frac{R_0}{R_n} + G_{S,DS} \cdot \frac{D_{S,P} \cdot R_0}{D_{S,N}} \tag{12}$$

Protozoan grazing on cyanobacteria is parameterized as:

$$G_{S,Cya} = G_{S0} \cdot \left(\frac{p_{SS} \cdot (P_{Cya})}{\begin{array}{c} K_{ZS} + p_{SS} \cdot (P_{Cya} + P_{UMD}) + p_{SL} \cdot (P_{Dtm} + P_{DDA} + D_{S,N}) \\ + p_{SZ} \cdot Z_S + p_{ST} \cdot P_{Tri} + p_{SD} \cdot D_{L,N} \end{array}} \right) \tag{13}$$

where K_s was the half-saturation constant for protozoans and p_{SS}, p_{SL}, p_{SZ}, $p_{ST,}$ and p_{SD} are the protozoan grazing preferences for cyanobacteria, diatoms, other protozoans, *Trichodesmium*, and large detritus, respectively. We allow for preferential grazing on the most abundant food source, which models a diverse community that adjusts to the dominant available prey. We formulate switching using the Stock and Dunne

BGD
10, 13931–13976, 2013

(2010) modification to the zooplankton grazing scheme of Fasham et al. (1990).

$$p_{SS} = \frac{\pi_{SS} \cdot (P_{Cya} + P_{UMD})}{\left\{ \begin{array}{c} (\pi_{SS} \cdot (P_{Cya} + P_{UMD}))^2 + (\pi_{SL} \cdot (P_{Dtm} + P_{DDA} + D_{S,N}))^2 \\ +(\pi_{ST} \cdot P_{Tri})^2 + (\pi_{SZ} \cdot Z_S)^2 + (\pi_{SD} \cdot D_{L,N})^2 \end{array} \right\}^{1/2}} \quad (14)$$

Mesozooplankton grow with a gross growth efficiency of γ_L, though they also have a basal metabolic rate of B_R. Mesozooplankton are grazed by an unmodeled higher predator that is assumed to co-vary with mesozooplankton and graze on them with the same Hollings Type 2 functional response used for the other grazers in the model (Stock and Dunne, 2010). Mesozooplankton are assumed to be capable of grazing on diatoms, protozoans, *Trichodesmium*, and detritus ($D_{L,P}$). As in the PISCES model (Aumont et al., 2003), we assume a lower maximum grazing rate for mesozooplankton than protozoans ($G_{L0} < G_{S0}$), which effectively limits the growth of mesozooplankton allowing their primary prey (diatoms) to escape grazing pressure while the protozoans keep the cyanobacteria population tightly controlled.

$$\frac{dZ_L}{dt} = \gamma_L \cdot GTL \cdot Z_L - B_R \cdot L_Z - m_{ZL} \cdot L_Z - \frac{G_{H0} \cdot Z_L \cdot Z_L}{K_H + Z_L} \quad (15)$$

$$GTL = G_{L,Dtm} + G_{L,DDA} \cdot \frac{R_0}{R_n} + G_{L,Tri} \cdot \frac{R_0}{R_n} + G_{LZ} + G_{L,DS} \frac{D_{S,P} \cdot R_0}{D_{S,N}} + G_{L,DL} \frac{D_{L,P} \cdot R_0}{D_{L,N}} \quad (16)$$

$$G_{L,Dtm} = G_{L0} \left(\frac{p_{LL} \cdot P_{Dia}}{K_{ZL} + p_{LL} \cdot (P_{Dtm} + P_{DDA} + D_{S,N}) + p_{LT} \cdot P_{Tri} + p_{LZ} \cdot Z_S + p_{LD} \cdot D_{L,N}} \right) \quad (17)$$

$$p_{LL} = \frac{\pi_{LL} \cdot (P_{DIA} + P_{DDA} + D_{S,N})}{\left\{ (\pi_{LL} \cdot (P_{Dtm} + P_{DDA} + D_{S,N}))^2 + (\pi_{LT} \cdot P_{Tri})^2 + (\pi_{LZ} \cdot Z_S)^2 + (\pi_{LD} \cdot D_{L,N})^2 \right\}^{1/2}} \quad (18)$$

Large detritus is produced as the egestion of mesozooplankton (ε = egestion efficiency). It is consumed by mesozooplankton, lost to the inorganic nutrient pool by

BGD
10, 13931–13976, 2013

bacterially mediated degradation, or lost as sinking flux (Appendix 2, Eq. A1). With respect to nitrogen, the increased N : P ratio of diazotrophs leads to an additional term representing the stoichiometrically unnecessary additional nitrogen (Eq. A2). We assume that all Si ingested by mesozooplankton passes directly to the detrital pool since zooplankton do not assimilate Si (Eq. A3).

A more slowly sinking detrital pool is composed of non-living diatom cells, that are produced through diatom mortality and lost to bacterially-mediated degradation to dissolved nutrients and sinking (Eqs. A4–6). Colloidal and dissolved detritus (D_S) is produced by a combination of protozoan egestion, excretion and sloppy feeding by both zooplankton groups (σ is the proportion of excretion and sloppy feeding that goes to the small detritus pool), exudation and mortality of all phytoplankton groups, and dissolution of large detritus. It is lost through bacterially mediated remineralization (Eq. A7). For colloidal detrital nitrogen we again have an additional component associated with the egestion and excretion of stoichiometrically unnecessary nitrogen (Eq. A8). Colloidal Si is derived from protozoan ingestion of diatoms and diatom mortality, as well as dissolution of large detritus (Eq. A9).

Nutrients (N and DIP) are regenerated through grazer excretion and bacterially mediated remineralization of colloidal and dissolved detritus (Eq. A10). We assume (following Hood et al., 2001) that diazotrophs take up DIN until they would be N-limited after which they fulfill the rest of their nitrogen budget with Nfix (Eq. A11). Si is generated only through the remineralization of detrital Si (Eq. A15). Parameter values used in our base run are shown in Table A1.

3 Results

3.1 Basin-scale model-data comparison

To remove errors introduced in point-to-point model-data comparisons by mesoscale variability, we have taken an integrative approach to model validation. In particular,

BGD
10, 13931–13976, 2013

we choose to compare the large-scale patterns and basin-scale rate measurements provided by individual studies to our model results. In this section we compare our model results to in situ measurements throughout the model domain, including Nfix, primary production (PP), and grazing rates. In the following section we will more directly compare our model results within the ARP to those measured by Subramaniam et al. (2008).

On north–south transects through the central North Atlantic, Fernandez et al. (2010) found that Nfix peaked at a mean of $\sim 60\,\mu mol\,N\,m^{-2}\,d^{-1}$ between 5° S and 15° N and averaged 25 and 11 $\mu mol\,N\,m^{-2}\,d^{-1}$ in the subtropical gyre for 2007 and 2008 respectively, while Moore et al. (2009) measured a relatively constant Nfix rate by unicellular diazotrophs of 16 $\mu mol\,N\,m^{-2}\,d^{-1}$, but a variable contribution by *Trichodesmium,* which peaked at $\sim 200\,\mu mol\,N\,m^{-2}\,d^{-1}$ between 5 and 15° N, but was less than 40 $\mu mol\,N\,m^{-2}\,d^{-1}$ north of 20° N. By comparison, the model predicts an annual mean value of 145 $\mu mol\,N\,m^{-2}\,d^{-1}$ for the central Atlantic (longitudinally) from 15° S to 30° N, increasing from a minuminum of 0.95 $\mu mol\,N\,m^{-2}\,d^{-1}$ at a coastal site in the northern region of the model to a peak in the ARP of 487 $\mu mol\,N\,m^{-2}\,d^{-1}$. In a study specifically focused on the tropical region from the equator to 15° N, Montoya et al. (2007) found that overall Nfix rates were not significantly different between the western (60–40° W, 201 $\mu mol\,N\,m^{-2}\,d^{-1}$) and eastern (40–20° W, 180 $\mu mol\,N\,m^{-2}\,d^{-1}$) regions, but that the role of unicellular diazotrophs increased significantly to the east. In our model, overall Nfix decreases slightly from west to east (255 $\mu mol\,N\,m^{-2}\,d^{-1}$ for the tropics west of 40° W and 179 $\mu mol\,N\,m^{-2}\,d^{-1}$ east of 40° W) and UMD reach a peak Nfix rate of $> 200\,\mu mol\,N\,m^{-2}\,d^{-1}$ within the Caribbean which was not sampled by Montoya et al. (2007), but maintain a relatively constant (and high) proportion of total Nfix throughout most of the horizontal band from 18° N to 25° N. Within the greater Mauritanian upwelling system (MUS, which we will define here as extending from the coast to 26° W and from 12° N to 30° N), Rijkenberg et al. (2011) measured mean surface Nfix rates of 0.3 $nmol\,N\,L^{-1}\,d^{-1}$ in January and February while in November and December Turk et al. (2011) measured significantly higher rates of 26.4 $nmol\,N\,L^{-1}\,d^{-1}$ although

BGD
10, 13931–13976, 2013

both studies agreed that Nfix was significantly higher in the south than the north. Our model predicted an annual mean surface value of 2.8 nmol N L^{-1} d^{-1} in the MUS, and a weak latitudinal trend. Overall, it appears that our model may underestimate the mean spatial variability in Nfix, although this may simply reflect high seasonal variability rectified in the model mean. Figure 2 clearly illustrates how high seasonal variability in the model is smoothed in the mean. A synthesis of in situ Nfix measurements compiled by Luo et al. (2012) exhibits much greater spatial heterogeneity than our 20 yr model mean. However, comparison to the lowest and highest Nfix months during the year 1990 (February and August, respectively) show that for the most part model variability comes close to matching the in situ variability, and matches the in situ data in finding highest Nfix rates in the ARP. Furthermore, it is interesting to note that the seasonal pattern of Nfix varies throughout the region. For instance, Gulf of Mexico Nfix values are very high in late summer, but negligible in winter, while Nfix values in the equatorial regions and off of Southern Africa are lower in August than February (Fig. 2).

In situ PP measurements typically suggest low rates of between 160 and 280 mg C m^{-2} d^{-1} in the oligotrophic subtropical gyre (Maranon et al., 2007; Perez et al., 2006; Teira et al., 2005; Tilstone et al., 2009). PP increases towards the equatorial and coastal upwelling regions, with typical values of 240–320 mg C m^{-2} d^{-1} in the equatorial region (Perez et al., 2005; Poulton et al., 2006) and 400–700 mg C m^{-2} d^{-1} in the MUS (Davenport et al., 2002; Neuer et al., 2002). In the model, primary productivity averages 225 mg C m^{-2} d^{-1} across the basin, varying from a mean of 168 mg C m^{-2} d^{-1} in the subtropical gyre to 325 mg C m^{-2} d^{-1} throughout the greater MUS, but peaking at an annual average of 1265 mg C m^{-2} d^{-1} near the coast in the MUS.

Across disparate regions of the global ocean, protistan grazing tends to constitute a relatively constant proportion of phytoplankton loss terms, varying from 60 % of PP in coastal environments to 75 % in tropical and subtropical regions (Calbet and Landry, 2004). Within the North Atlantic subtropical gyre, Quevedo and Anadón (2001) found protistan grazing rates of 78 % PP at the surface and 109 % at the deep chlorophyll max. Across the model domain, protistan grazing averaged 71 % of particulate PP,

BGD
10, 13931–13976, 2013

varying from a minimum integrated annual average of 40–60 % in the coastal eutrophic regions to a maximum integrated annual average of ~ 90 % in core of the oligotrophic gyre. Globally, mesozooplankton grazing averages ~ 12 % PP (Calbet, 2001), although variability is extremely high. On a series of north–south transects through our study region, Huskin et al. (2001) measured copepod gut pigments and found that grazing ranged from an average of 4 % PP in the subtropical gyre to 23 % PP in the tropics, while Isla et al. (2004) measured grazing rates ranging from 4–5 % PP in the tropics and subtropical gyre to 16 % in the MUS. Lopez and Anadón (2008) concurred with this general pattern, but found significantly higher rates of 26–112 % PP in the gyre and higher in upwelling regions. Conversely, Calbet et al. (2009) conducted mesozooplankton incubations and found higher relative grazing rates of 28 % PP in the gyre than in the MUS (6 % PP) or the tropics (17 % PP). The model showed relatively high mesozooplankton grazing rates that averaged 27 % PP across the domain, varying from a minimum integrated annual average of < 10 % in the core of the oligotrophic gyre to a maximum integrated annual average of > 40 % in the equatorial and coastal regions.

3.2 Amazon River Plume regional model-data comparison

The ARP is a region with high spatiotemporal variability in its physics, biogeochemistry, ecology, and sheer extent. In situ Nfix rate measurements have been concentrated in the northern summer from April to October when plume area is greatest (Hu et al., 2004) and our model predicts the highest mean ARP Nfix. Cruises in the region have measured widely differing rates of Nfix and documented different roles for the dominant diazotrophs in the ARP. Cruise tracks have typically been biased towards bloom regions, and Nfix within these blooms reaches very high rates. DDA blooms have been encountered with average Nfix rates of 3200 $\mu mol\,N\,m^{-2}\,d^{-1}$ (Carpenter et al., 1999). Nfix by *Trichodesmium* in the region can also reach rates exceeding 1000 $\mu mol\,N\,m^{-2}\,d^{-1}$, although cruise means typically vary from 50 to 300 $\mu mol\,N\,m^{-2}\,d^{-1}$ (Capone et al., 2005; Montoya et al., 2007). UMD Nfix rates are

BGD
10, 13931–13976, 2013

generally lower, ranging from 20–50 $\mu mol\,N\,m^{-2}\,d^{-1}$ (Falcon et al., 2004; Montoya et al., 2007). Meanwhile, Subramaniam et al. (2008) measured mean Nfix rates (by acetylene reduction) throughout the region of 98 $\mu mol\,N\,m^{-2}\,d^{-1}$ for *Trichodesmium* and 49 $\mu mol\,N\,m^{-2}\,d^{-1}$ for DDA, although they believe that the acetylene reduction vastly underestimated the Nfix of DDA, because at mesohaline regions dominated by DDA, $^{15}N_2$ uptake measurements suggested vastly higher Nfix rates of 986 $\mu mol\,N\,m^{-2}\,d^{-1}$. For all taxa and studies, however, these high mean rates are often driven by a few extreme values. For instance, although the mean Nfix at mesohaline regions measured by Subramaniam et al. (2008) was 986 $\mu mol\,N\,m^{-2}\,d^{-1}$, the median value was only 82 $\mu mol\,N\,m^{-2}\,d^{-1}$. This high patchiness is not exhibited in the model, and remains a challenge for modelers in general.

Nevertheless it is possible to draw some broad generalizations from the existing in situ measurements. Subramaniam et al. (2008) defines three distinct subregions: low-salinity (SSS < 30), mesohaline (30 < SSS < 35), and oceanic (SSS > 35). The low salinity region is a light-limited region with a shallow euphotic zone and a phytoplankton community dominated by coastal diatoms and negligible Nfix. The mesohaline region exhibits high P : N and Si : N ratios, which stimulates Nfix by DDA, although with additional contributions from *Trichodesmium*. The oceanic region is relatively depleted in Si and dominated by *Trichodesmium* and other cyanobacteria.

While Subramaniam et al. (2008) restricted their study to a latitudinal band from 0–15° N, we will consider the ARP region as extending from 60° W to 40° W and 0–20° N based on our model result that Nfix often peaked north of 15° N, a result that actually agrees well with the results of Capone et al. (2005) and is supported by Coles et al. (2013) who found high penetration of Amazon River water into the Caribbean. Our model predicted annual mean Nfix in the ARP of 275 $\mu mol\,N\,m^{-2}\,d^{-1}$. The low-salinity region had lower Nfix rates (204 $\mu mol\,N\,m^{-2}\,d^{-1}$) and a community dominated by non-diazotrophic diatoms (49 % of total biomass, Fig. 3). In the mesohaline region mean Nfix was 372 $\mu mol\,N\,m^{-2}\,d^{-1}$ (compared to a median of 334 $\mu mol\,N\,m^{-2}\,d^{-1}$ and a maximum of 3050 $\mu mol\,N\,m^{-2}\,d^{-1}$), suggesting that our model may have accurately

BGD
10, 13931–13976, 2013

captured the average conditions in the region, but perhaps missed some of the extreme blooms encountered by Subramaniam et al. (2008). Nfix was fueled by DDA in this region (Fig. 4) which were responsible for 299 $\mu mol\,N\,m^{-2}\,d^{-1}$ and contributed 10 % of biomass (compared to 28 % estimated by Subramaniam et al., 2008). While DDA blooms were largely restricted to the mesohaline region, their concentrations within this salinity region were seasonally variable (Fig. 5). Within the high-salinity oceanic region, DDA contributed only 3.4 % of biomass (compared to < 2 % estimated by Subramaniam et al., 2008) and *Trichodesmium* dominated Nfix, contributing 48 % of the total 213 $\mu mol\,N\,m^{-2}\,d^{-1}$, while total biomass was dominated by the cyanobacteria (including *Trichodesmium*, UMD, and Cya), which together accounted for 65 % of the biomass. Mean annual patterns of diazotroph biomass in the model suggested that both *Trichodesmium* and DDA peaked in the northwestern ARP, although *Trichodesmium* seems to monotonically decrease gradually from a maximum in the Caribbean, while DDA peak in the region from 10–17° N and 60 to 50° W (Fig. 5). These general patterns agree reasonably well with the measurements of Subramaniam et al. (2008), although their cruise tracks did not extend north of 15° N and the large scatter in the field measurements exhibits a much larger range of variability for *Trichodesmium* than predicted by our annual mean values.

By defining the ARP as a system of communities with varying degrees of mixing between the river and ocean water, we can use the salinity gradient to compare our model to the measurements of Subramaniam et al. (2008). Our model seems to accurately depict Si as a function of salinity (Fig. 4b). DIN : DIP ratios in the model showed less variability than the in situ measurements, though surface measured nutrients were typically near detection limits, and hence there is large uncertainty in the ratio of the measured values (Fig. 4a). The model also generally agreed with in situ DDA Nfix measurements, though it did not produce some of the highest values of Tricho Nfix measured (Fig. 4d). The model predicted lower primary productivity in the low salinity regions than the in situ data (230 compared to 420 $mg\,C\,m^{-2}\,d^{-1}$), although it is worth noting that Subramaniam et al. (2008) only sampled two stations with salinity < 27 (and

BGD
10, 13931–13976, 2013

only one with detectable NO_3) and hence likely missed the early phase of the coastal blooms. Through the rest of ARP, the in situ data suggested primary production of $\sim 700\,mg\,C\,m^{-2}\,d^{-1}$, with no distinct trend with salinity. Our model also suggested similarity in primary production in the meso- and oligohaline regions, but with much lower values of 188 and $163\,mg\,C\,m^{-2}\,d^{-1}$, respectively.

3.3 Phytoplankton succession in a Lagrangian framework

Utilizing synthetic surface floats in HYCOM, we follow model parcels of river water as they were advected into the WTNA and assess phytoplankton successional patterns within a Lagrangian framework. Focusing on the year 1991 (determined by Coles et al., 2013 to be a typical plume year), we released sets of 25 floats from randomized locations within a 500 km wide by 150 km thick box near the river mouth every five days. Each float was tracked for six months, with floats that ran aground within 6 months of release excluded from the following analysis (Fig. 6a).

Successional patterns along the float trajectories exhibited repeatable patterns with coastal diatom blooms typically initiated within 15 days of float release. Coastal diatom blooms were associated with drawdown of DIN. Meanwhile, since DIP : DIN and Si : DIN ratios in river water were in excess of Redfield, DIP and Si exhibited patterns that suggested near conservative mixing between high nutrient river water and oligotrophic oceanic water. While cyanobacteria biomass sometimes peaked during the diatom blooms, its variability was much lower than that of diatoms. Relative contribution of cyanobacteria to total biomass was significantly greater in offshore regions. *Trichodesmium* typically peaked offshore (though occasional strong blooms occurred immediately after float release), often reaching highest biomass as many as three months after release of the float. Unicellular diazotrophs seldom reached substantial concentrations in floats released at the river mouth, and only bloomed several months after release.

In contrast to the highly repeatable patterns found for the other phytoplankton groups, DDA blooms were variable both in their timing and presence along float trajectories

BGD
10, 13931–13976, 2013

(Fig. 6b). While 25 % of float trajectories never exceeded 0.085 µmol DDA N L^{-1}, another 25 % exhibited DDA blooms with maximum biomass > 0.20 µmol N L^{-1}. If we define this upper quartile as the float trajectories that experienced strong DDA blooms, we can begin to look at the factors controlling DDA growth. While 95 % of blooms reached their peak within 75 days of release, within this window there was wide variability in the timing of the blooms. The median duration to bloom peak was 37.5 days, however 25 % of the blooms reached their peak within 22 days of release and another quarter of the blooms required 50 days to reach their peak.

While the variability in bloom timing makes it difficult to compare bloom dynamics in the temporal domain, blooms followed repetitive trajectories in the salinity domain indicating high variability in physical plume entrainment rates. A small proportion of floats experience DDA blooms at lower salinities, however most blooms are initiated at salinities > 25 and reach peaks in salinity ranges from 30–32. This allows us to average multiple bloom trajectories in the salinity domain to assess the factors controlling bloom formation.

DDA specific growth rates were highest near the river mouth where abundant nutrients led to average rates of 0.8 d^{-1} (Fig. 7a). They remained high until salinity reached ~ 25. At this point decreasing dissolved Si concentrations, driven primarily by mixing with low Si oceanic water, caused a rapid decrease in DDA specific growth rates, which continued to drop until they reached values < 0.2 d^{-1} in oceanic water. Surprisingly, the strong decrease in DDA growth rates from salinities of 25 to > 35 corresponded with the region of strongest bloom formation. This apparent discrepancy is explained when comparing specific growth rates to specific mortality rates. While growth rates decrease only slowly with increasing salinity within the salinity band from of 0–20, DDA specific mortality rates decrease roughly linearly with salinity. Mortality near the river mouth (Fig. 7b), driven by grazing of high concentrations of mesozooplankton supported by the coastal diatom populations, exceeded DDA growth rates. In the salinity range from 15–20, mortality decreased significantly to allow a net positive growth rate for DDA, which then reached a maximum in net growth rate in the salinity band from

BGD
10, 13931–13976, 2013

25–30 coinciding with the range where most blooms were initiated. At salinities > 32 decreasing net growth rates (resulting from the sharply declining specific growth rates as Si-limitation was induced), combined with physical dilution of the mesohaline water, led to bloom termination.

While this simple story of cessation of top-down pressure leading to bloom formation and bottom-up pressure causing bloom termination is appealing, it is not the full story. If we similarly compare specific growth and mortality rates along the float trajectories that did not experience DDA blooms (defined here as the float trajectories with max DDA concentrations < 0.085 – e.g. the lower quartile), we find growth and mortality rates that closely match those found in the strong bloom floats (Fig. 7c). In fact, the average net growth rates in the optimal salinity band of the non-bloom floats are slightly higher than those in the bloom floats. The primary difference between the bloom and non-bloom floats was not in biological and chemical forcing, but rather in the physical transport and mixing rates. Bloom floats spent a significantly longer duration in the mesohaline region than non-bloom floats (Fig. 8), implying weaker vertical and/or horizontal mixing of oceanic water into the plume water for the bloom floats. The median length of time spent by non-bloom floats in the key salinity range of 20–34 was only 16 days, while all floats that experienced strong blooms spent at least 23 days in this salinity range (Fig. 8b). Only 5 % of non-bloom floats spent 56 days in this salinity range, while half of the bloom floats spent longer than that period. The importance of an extended time period spent in the ideal habitat range of the DDA is apparent from the small net growth rates of DDA (Fig. 7c). If we assume a net growth rate of 1.1 d^{-1}, it would take 25 days for DDA concentrations starting at the ARP region median value of 0.02 $\mu mol N L^{-1}$ to reach strong bloom values of 0.2 $\mu mol N L^{-1}$, if we assume no losses to diffusion. Obviously, vertical and horizontal diffusive losses of DDA from the core of the bloom could substantially increase the time required for bloom growth.

BGD
10, 13931–13976, 2013

3.4 Sensitivity analysis

To assess the sensitivity of our model to parameter selections, we repeatedly ran the model over a four month period (beginning in May), which corresponded to the primary model bloom formation period in 1991, while sequentially varying ecological model parameters (Fig. 9, Table A1). In order to preserve niche space for each phytoplankton taxa, rather than individually scaling max phytoplankton growth rates, we re-wrote diatom and DDA max growth rates as:

$$\mu_{\text{large}} = \mu_{\text{small}} + \delta_{\text{large:small}} \times \mu_{\text{small}} \quad (19)$$

$$\mu_{\text{DDA,max}} = \mu_{\text{large}} \times \vartheta_{\text{L}} = \mu_{\text{large}} + \delta_{\text{DDA:Dtm}} \times \mu_{\text{large}} \quad (20)$$

$$\mu_{\text{DDA,nif}} = \mu_{\text{large}} \times \vartheta_{\text{nif}} = \mu_{\text{DDA}} + \delta_{\text{nif,max}} \times \mu_{\text{DDA}} \quad (21)$$

and varied μ_{small} (which varies all phytoplankton growth rates proportionally), $\delta_{\text{large:small}}$ (varies the ratio of Diatom and DDA to cyanobacterial growth), $\delta_{\text{DDA:Dtm}}$ (varies the ratio of DDA to Dtm growth). We varied ϑ_{nif} directly since it does not impact DDA max growth rates, but instead their max diazotrophic growth rates. In each simulation, we compared variability in key model standing stocks and rates both in the ARP and across the entire basin (Fig. 9).

Sensitivity analysis showed that the model was roughly equally sensitive to parameters affecting bottom-up and top-down control of phytoplankton (Fig. 9). The model was particularly susceptible to variations in both the absolute magnitude of phytoplankton growth rates (μ_{small}, Eq. 19) and the ratio of large : small phytoplankton growth rates ($\delta_{\text{large:small}}$, Eq. 19), and the growth rates (G_{S0}, G_{L0}) and half-saturation constants (K_{ZS}, K_{ZL}) for both zooplankton size classes. Surprisingly, over the four month runs of our sensitivity analysis simulations, the model was relatively insensitive to changes in riverine nutrient concentrations. Nfix was almost completely insensitive to changes in riverine phosphate concentrations, although this was likely due to the short duration of our simulations, combined with the fact that the two dominant taxa in the ARP (diatoms and DDA) were not P-limited. In contrast to other phytoplankton taxa, DDA re-

BGD
10, 13931–13976, 2013

sponded similarly to all changes in phytoplankton growth rates with increases in μ_{small}, $\delta_{large:small}$, $\delta_{DDA:Dtm}$, and ϑ_{nif} all leading to increases in DDA concentration. Decreases in K_{LSi} positively affected DDA concentrations, while decreases in K_{LN} led to decreases in DDA concentrations, likely due to increased Si utilization by Dtm. The model was insensitive to changes in K_{SP}, because diatoms were not P-limited. Altered intrinsic mortality rates had minimal effect on the model, reflecting the fact that phytoplankton were primarily lost to grazers. Overall, the similar sensitivity of the model to phytoplankton growth and zooplankton grazing parameters supports our conclusion that both bottom-up and top-down forcing play a role in DDA blooms.

4 Discussion

4.1 Modeling diazotroph distributions

Global and basin-scale models of diazotrophy have typically focused on *Trichodesmium*, a colonial cyanobacterium that grows slowly and is assumed to sustain low (if any) grazing mortality. As a result, these models often contain simplified grazing parameterizations and instead focus solely on bottom-up forcing of growth rates by phosphate and organic phosphorus availability (Ye et al., 2012), temperature (Breitbarth et al., 2007; Moore et al., 2002), and Fe deposition (Coles and Hood, 2007; Moore et al., 2006). Our model differs significantly from these previous efforts in focusing on DDA, whose distributions may be controlled in part by predation pressure from mesozooplankton, ciliates, and other protozoa. Furthermore, in focusing specifically on the ARP region, we have been able to neglect other factors contributing to global diversity of diazotrophs. In particular, temperature is relatively constant throughout our latitudinally restricted domain and Fe is unlikely to be limiting in the plume region, though our decision not to include Fe-limitation may explain the model's tendency to overestimate nitrogen fixation in the eastern tropical North Atlantic.

BGD
10, 13931–13976, 2013

While most previous models contained a single diazotroph state variable, our requirement that this model maintain populations of three distinct diazotrophs (*Trichodesmium*, DDA, and unicellular microbial diazotrophs) necessitated the definition of three distinct niche spaces. Unfortunately, while *Trichodesmium* has been relatively well studied both in the field and in the laboratory, few comparable studies have addressed growth rates and limiting nutrients of DDA and UMD. The experimental evidence that exists suggests that both *Crocosphaera* (a UMD; Dekaezemacker and Bonnet, 2011) and diatom-*Richelia* symbioses (Foster et al., 2011; Villareal, 1990) have growth rates that are slower than equivalent non-diazotrophic taxa (by which we mean total non-diazotrophic cyanobacteria and diatoms, respectively). Without any compelling evidence to believe that UMD and DDA behave differently with respect to light or nutrient uptake kinetics (excepting N), we thus chose to model them as identical to their non-diazotrophic counterparts in these respects.

To understand how these a priori constraints on the phytoplankton community translated into realized niches in the model, we utilized principle component analysis (PCA) to determine the relationships between the three nutrients and 7 plankton state variables in the model (Fig. 10). The first principle component (accounting for 39.5 % of the variance) primarily divided the dataset into nutrient-rich and oligotrophic regions, with diatoms and both types of zooplankton co-varying with nutrients while UMD and *Trichodesmium* were inversely correlated with nutrients on this axis. The second, and particularly third, principle components (accounting for 15.8 and 12.7 % of the variance, respectively) begin to separate the diazotroph classes more effectively. Both PC2 and PC3 separate the nutrients based primarily on DIP : DIN ratios. In each case DDA covary with the DIP : DIN ratio. Along PC2, DIP and Si are correlated with each other and with all three of the diazotrophs. PC3, however, strongly differentiates the diazotrophs with DDA correlating with high DIP : DIN ratios (and a similar loading score to cyanobacteria), *Trichodesmium* showing near zero loading, and UMD exhibiting a negative loading score. Overall this PCA shows that diatoms occupy the high nutrient niche in the model. Cya and DDA both exist at intermediate nutrient levels, with

BGD
10, 13931–13976, 2013

DDA specializing in high DIP : DIN ratios and cyanobacteria preferring low DIP : DIN. *Trichodesmium* and UMD are both low nutrient specialists, with *Trichodesmium* preferring the high DIP : DIN regions and UMD excelling in the most nutrient poor regions. Interestingly, there was almost no niche overlap between diatoms and DDA or between Cya and UMD. In each of the first three principal components these pairs were negatively correlated, perhaps because the similar grazing pressure experienced by both types of diatoms or by both types of unicellular cyanobacteria inhibited coexistence.

4.2 Determinants of phytoplankton succession

Phytoplankton bloom succession in the ARP is governed by a complex inter-play of physical, bottom-up, and top-down forcing mechanisms. Given the complexity of the three-dimensional physical circulation model, it is instructive to consider successional patterns in a simplified conceptual framework. The Amazon River introduces tremendous quantities of nutrient-rich water to the WTNA, but the nitrate in this source water exists at sub-Redfield ratios, and hence is quickly drawn down by blooms of coastal diatoms. This leaves nitrate-depleted, but DIP- and Si-rich, water that is ideal for DDA growth.

The DIP- and Si-rich water is entrained into the oligotrophic waters of the WTNA with mixing rates that are dependent both on the magnitude of river flux and the wind-driven circulation of the WTNA (Coles et al., 2013). In fact, Fig. 4 suggests that Si concentrations can be approximated by a conservative mixing assumption. Furthermore, mesozooplankton (the dominant loss term for DDA, Fig. 7) co-varies with Si (Fig. 10). Mesozooplankton reach maximal concentrations in the coastal blooms near the river mouth and also exhibit a decline in concentration that can be approximated by a conservative mixing assumption. DDA net growth rates as a function of salinity can thus be estimated by considering the functional responses of DDA to nutrients and predators, while the concentrations of both of these state variables are controlled primarily by identical physical mixing processes. We have parameterized DDA response to Si as a monod-type response (Eq. 8), thus the nutrient-limited growth rates of DDA

BGD
10, 13931–13976, 2013

decrease only slowly at low salinity/high Si, until Si drops to concentrations near the half-saturation constant for DDA (2.0 $\mu mol L^{-1}$) at a salinity of ~ 34 (Fig. 11). After this point, growth rates begin to decrease much more rapidly. At the same time, for this simple conceptual model, we consider mesozooplankton to have the same primary loss term (dilution by low concentration oceanic water) as Si. However, the phytoplankton functional response to predators is drastically different than that to nutrients. For a given phytoplankton concentration, phytoplankton loss rates will vary linearly with zooplankton concentration (Eq. 7), creating a mesohaline region where growth exceeds grazing. Mesohaline DDA blooms are thus an emergent property that arises from the shape of the transfer functions relating DDA to nutrients and zooplankton, combined with the physically-driven linear loss rates of both Si and mesozooplankton along the salinity gradient. The crucial importance of these functional responses highlights the importance of both in situ and laboratory experiments to determine the response of DDA to varying nutrient concentrations and grazing rates of zooplankton on DDA.

Despite the attractive simplicity of this mechanism, it is important to point out that our model only shows that such a mechanism could account for the prevalence of DDA in the mesohaline regions of the ARP. Other mechanisms may plausibly create a similar pattern. For instance, DDA have at times been observed at high concentrations in the dark regions immediately beneath the plume (J. Goes, personal communication, 2012), which may suggest an adaptation to lower light conditions than most diatoms. DDA also at times occur in regions with anomalously high (relative to conservative mixing with salinity) total phosphorus concentrations, which may suggest a utilization of other forms of phosphorus by DDA or other taxa with which they co-occur. Utilization of DOP by alkaline-phosphatase containing diazotrophs has been included in several previous models (e.g. Coles and Hood, 2007), but was excluded in ours.

Furthermore, our model predicts an overly rhythmic seasonal pattern, lacking the interannual variability in DDA phenology found in the ARP, and fails to produce rare, exceptionally dense blooms of all phytoplankton taxa. Inclusion of interannual variability in timing and magnitude of Amazon River discharge and seasonal variability in

BGD
10, 13931–13976, 2013

river nutrient concentrations may begin to explain some of these model–data discrepancies. Nevertheless, it seems that some additional mechanisms may be necessary to increase the model variance in DDA concentration. Of particular importance might be variability in mesozooplankton grazing pressure, perhaps induced by life history characteristics of dominant grazers, selectivity for or switching between diatom prey species, or density-dependent predator defense mechanisms.

DDA have been suggested to play a distinct biogeochemical role due to their unique potential for both diazotrophy and mineral ballast driven rapid sinking rates (Subramaniam et al., 2008). In fact, massive DDA blooms have been found to co-occur with regions of high pCO_2 drawdown in situ, supporting the important role of DDA in ARP biogeochemistry (Cooley and Yager, 2006). Within the ARP region of our model, nitrogen fixation by DDA can support 35.4 % of the nitrogen exported across the 100 m depth horizon by sinking particles. Variability is high, however, with ARP region values ranging from 1.2 % to 116 % of export, and intra-regional variability even higher. Nevertheless, it is clear that DDA introduce a significant fraction of the ARP region's new production, and hence may contribute significantly to regional carbon drawdown.

5 Conclusions

This is the first biogeochemical model to specifically investigate DDA populations, and with that goal came the need to parameterize zooplankton grazing in an explicit manner that is not typically utilized with models focused on diazotrophy. While our model generally agrees with the Subramaniam et al. (2008) assertion that DDA bloom in mesohaline regions with high P and Si and depleted DIN, it uncovers two additional prerequisites for bloom formation. The first is a cessation of grazing pressure due to dilution of the high coastal zooplankton abundance with oceanic, lower zooplankton abundance water. The second is a significant retention time within the mesohaline region. Unfortunately, due to the paucity of experimental evidence about DDA growth kinetics and grazing rates on DDA, model functional parameterization was largely unconstrained

BGD
10, 13931–13976, 2013

by the existing data, and alternative forms of grazing and nutrient limitation functions may have been equally valid. Nevertheless the interplay of top-down, bottom-up, and physical forcing on DDA discovered in our model can be framed as three testable hypotheses: (1) DDA specific gross growth rates will be highest near the river mouth (or in high nutrient water) and decrease along the salinity (nutrient) gradient with the greatest decreases in growth rate occurring at a salinity > 32. (2) DDA specific grazing losses to mesozooplankton will be highest in the oligohaline water and decrease with increasing salinity. (3) DDA net growth rates in the mesohaline region will be low, necessitating low physical mixing rates and high retention of water parcels in the mesohaline region in order for bloom initiation. Further experimental evidence is necessary to ascertain the veracity of these mechanisms of bloom formation. It is also important to note that these prerequisites for bloom formation are likely not specific to DDA. Niche spaces for all phytoplankton taxa are a function of inequity in growth and mortality, and the duration of time spent in these niche spaces may be as critical to bloom formation as the magnitude of the growth-grazing imbalance.

Appendix A

Nutrient and detritus equations

$$\frac{dD_{L,P}}{dt} = \frac{\varepsilon_L}{R_0}\cdot GTL\cdot Z_L + \frac{\varepsilon_H}{R_0}\cdot\frac{G_{H0}\cdot Z_L\cdot Z_L}{K_H+Z_L} - \frac{G_{L,DL}}{R_0}\cdot Z_L - \epsilon_{DLP,DIP}\cdot D_{L,P} - \omega_L\cdot D_{L,P} \quad (A1)$$

$$\frac{dD_{L,N}}{dt} = \varepsilon_L\cdot GTL\cdot Z_L + \varepsilon_L\cdot\left\{G_{L,DDA}+G_{L,Tri}\right\}\cdot\left(1-\frac{R_0}{R_N}\right)\cdot Z_L + \varepsilon_L\cdot G_{L,DS} \cdot\left(1-\frac{R_0\cdot D_{S,P}}{D_{S,N}}\right)\cdot Z_L + \varepsilon_L\cdot G_{L,DS}\cdot\left(1-\frac{R_0\cdot D_{S,P}}{D_{S,N}}\right)\cdot Z_L + \varepsilon_H\cdot\frac{G_{H0}\cdot Z_L\cdot Z_L}{K_H+Z_L} - G_{L,DL}\cdot Z_L - \epsilon_{DSN,DIN}\cdot D_{L,N} - \omega_L\cdot D_{L,N} \quad (A2)$$

BGD
10, 13931–13976, 2013

$$\frac{dD_{L,Si}}{dt} = \frac{G_{L,Dtm}}{R_{Si}} \cdot Z_L + \cdot \frac{G_{L,DDA}}{R_{Si}} \cdot Z_L + \frac{D_{S,Si}}{D_{S,N}} G_{L,DS} \cdot Z_L + \frac{D_{L,Si}}{D_{L,N}} G_{L,DL} \cdot Z_L$$
$$- \frac{D_{L,Si}}{D_{L,N}} G_{L,DL} \cdot Z_L - \epsilon_{DLSi,Si} \cdot D_{L,Si} - \omega_L \cdot D_{L,Si} \quad \text{(A3)}$$

$$\frac{dD_{S,P}}{dt} = \frac{m_P}{R_0} \cdot f \cdot P_{Dtm} + \frac{m_P}{R_N} \cdot f \cdot P_{DDA} - \frac{G_{S,DS} \cdot D_{S,P}}{D_{S,N}} \cdot Z_S - \frac{G_{L,DS} \cdot D_{S,P}}{D_{S,N}} \cdot Z_L$$
$$- \epsilon_{DSP,DIP} \cdot D_{S,P} - \omega_S \cdot D_{S,P} \quad \text{(A4)}$$

$$\frac{dD_{S,N}}{dt} = m_P \cdot f \cdot P_{Dtm} + m_P \cdot f \cdot P_{DDA} - G_{S,DS} \cdot Z_S - G_{L,DS} \cdot Z_L$$
$$- \epsilon_{DSN,DIN} \cdot D_{S,N} - \omega_S \cdot D_{S,N} \quad \text{(A5)}$$

$$\frac{dD_{S,Si}}{dt} = \frac{m_P}{R_{Si}} \cdot f \cdot P_{Dtm} + \frac{m_P}{R_{Si}} \cdot f \cdot P_{DDA} - \frac{G_{S,DS} \cdot D_{S,Si}}{D_{S,N}} \cdot Z_S - \frac{G_{L,DS} \cdot D_{S,Si}}{D_{S,N}} \cdot Z_L$$
$$- \epsilon_{DSP,DIP} \cdot D_{S,P} - \omega_S \cdot D_{S,P} \quad \text{(A6)}$$

$$\frac{dD_{C,P}}{dt} = \frac{(1 - \gamma_L - \varepsilon_L)\sigma_L}{R_0} \cdot GTL \cdot Z_L + \frac{(1 - \varepsilon_H)\sigma_H}{R_0} \cdot \frac{G_{H0} \cdot Z_L \cdot Z_L}{K_H + Z_L}$$
$$+ \frac{(1 - \gamma_S - \varepsilon_S)\sigma_S + \varepsilon_S}{R_0} \cdot GTS \cdot Z_S$$
$$+ (1 - \alpha) \cdot \left(U_{Cya} \cdot \frac{P_{Cya}}{R_0} + V_{UMD} \cdot \frac{P_{UMD}}{R_N} + U_{Dtm} \cdot \frac{P_{Dtm}}{R_0} + V_{DDA} \cdot \frac{P_{DDA}}{R_N} + V_{Tri} \cdot \frac{P_{Tri}}{R_N} \right)$$
$$+ \left(m_P \cdot \frac{P_{Cya}}{R_0} + m_P \cdot \frac{P_{UMD}}{R_N} + m_P \cdot (1 - f) \cdot \frac{P_{Dtm}}{c} + m_P \cdot (1 - f) \cdot \frac{P_{DDA}}{R_N} + m_P \cdot \frac{P_{Tri}}{R_N} \right)$$
$$- \epsilon_{DCP,DIP} \cdot D_{C,P} \quad \text{(A7)}$$

$$\frac{dD_{C,N}}{dt} = (1 - \gamma_L - \varepsilon_L)\sigma_L \cdot GTL \cdot Z_L + (1 - \varepsilon_H)\sigma_H \cdot \frac{G_{H0} \cdot Z_L \cdot Z_L}{K_H + Z_L}$$

BGD
10, 13931–13976, 2013

$$+\left((1-\gamma_S-\varepsilon_S)\,\sigma_S+\varepsilon_S\right)\cdot \mathrm{GTS}\cdot Z_S+(1-\varepsilon_L)\,\sigma_L\cdot\left\{G_{L,DDA}+G_{L,Tri}\right\}\cdot\left(1-\frac{R_0}{R_N}\right)\cdot Z_L$$

$$+(1-\varepsilon_L)\,\sigma_L\cdot\left\{G_{L,DS}\cdot\left(1-\frac{R_0\cdot D_{S,P}}{D_{S,N}}\right)+G_{L,DL}\cdot\left(1-\frac{R_0\cdot D_{S,P}}{D_{S,N}}\right)\right\}\cdot Z_L$$

$$+\left((1-\varepsilon_S)\,\sigma_S+\varepsilon_S\right)\cdot\left\{G_{S,UMD}+G_{S,DDA}+G_{S,Tri}\right\}\cdot\left(1-\frac{R_0}{R_N}\right)\cdot Z_S$$

$$+\left((1-\varepsilon_S)\,\sigma_S+\varepsilon_S\right)\cdot G_{S,DS}\cdot\left(1-\frac{R_0\cdot D_{S,P}}{D_{S,N}}\right)\cdot Z_S$$

$$+(1-\alpha)\cdot\left(U_{Cya}\cdot P_{Cya}+V_{UMD}\cdot P_{UMD}+U_{Dtm}\cdot P_{Dtm}+V_{DDA}\cdot P_{DDA}+V_{Tri}\cdot P_{Tri}\right)$$

$$+\left(m_P\cdot P_{Cya}+m_P\cdot P_{UMD}+m_P\cdot(1-f)\cdot P_{Dtm}+m_P\cdot(1-f)\cdot P_{DDA}+m_P\cdot P_{Tri}\right)$$

$$+m_z\cdot Z_S+m_z\cdot Z_L-\epsilon_{DCN,DIN}\cdot D_{C,N} \tag{A8}$$

$$\frac{\mathrm{d}D_{C,Si}}{\mathrm{d}t}=R_{Si,Dtm}\cdot G_{S,Dtm}+R_{Si}\cdot G_{S,DDA}+\frac{m_P\cdot(1-f)}{R_{Si}}\cdot P_{Dtm}$$

$$+\frac{m_P\cdot(1-f)}{R_{Si}}\cdot P_{DDA}-\epsilon_{DCSi,Si}\cdot D_{C,Si} \tag{A9}$$

$$\frac{\mathrm{dDIP}}{\mathrm{d}t}=\frac{(1-\gamma_L-\varepsilon_L)(1-\sigma_L)}{R_0}\cdot\mathrm{GTL}\cdot Z_L+\frac{(1-\varepsilon_H)(1-\sigma_H)}{R_0}\cdot\frac{G_{H0}\cdot Z_L\cdot Z_L}{K_H+Z_L}$$

$$+\frac{(1-\gamma_S-\varepsilon_S)(1-\sigma_S)}{R_0}\cdot\mathrm{GTS}\cdot Z_S+\epsilon_{DCP,DIP}\cdot D_{C,P}+\epsilon_{DSP,DIP}\cdot D_{S,P}$$

$$+\epsilon_{DLP,DIP}\cdot D_{L,P}-\frac{U_{Cya}}{R_0}\cdot P_{Cya}-\frac{V_{UMD}}{R_N}\cdot P_{UMD}-\frac{U_{Dtm}}{R_0}\cdot P_{Dtm}$$

$$-\frac{G_{DDA}}{R_N}\cdot P_{DDA}-\frac{U_{Tri}}{R_N}\cdot P_{Tri} \tag{A10}$$

$$\frac{\mathrm{dDIN}}{\mathrm{d}t}=(1-\gamma_L-\varepsilon_L)(1-\sigma_L)\cdot\mathrm{GTL}\cdot Z_L+(1-\varepsilon_H)(1-\sigma_H)\cdot\frac{G_{H0}\cdot Z_L\cdot Z_L}{K_H+Z_L}$$

BGD
10, 13931–13976, 2013

$$+(1-\gamma_S-\varepsilon_S)(1-\sigma_S)\cdot \mathrm{GTS}\cdot Z_S+(1-\varepsilon_L)(1-\sigma_L)\cdot\left\{G_{L,\mathrm{DDA}}+G_{L,\mathrm{Tri}}\right\}\cdot\left(1-\frac{R_0}{R_N}\right)$$

$$\cdot Z_L+(1-\varepsilon_L)(1-\sigma_L)\cdot\left\{G_{L,\mathrm{DS}}\cdot\left(\frac{D_{S,N}}{D_{S,P}}-R_0\right)+G_{L,\mathrm{DL}}\cdot\left(1-\frac{R_0\cdot D_{S,P}}{D_{S,N}}\right)\right\}\cdot Z_L$$

$$+(1-\varepsilon_S)(1-\sigma_S)\cdot\left\{G_{S,\mathrm{UMD}}+G_{S,\mathrm{DDA}}+G_{S,\mathrm{Tri}}\right\}\cdot\left(1-\frac{R_0}{R_N}\right)\cdot Z_S$$

$$+(1-\varepsilon_S)(1-\sigma_S)\cdot G_{S,\mathrm{DS}}\cdot\left(1-\frac{R_0\cdot D_{S,P}}{D_{S,N}}\right)\cdot Z_S+\epsilon_{\mathrm{DCN,DIN}}\cdot D_{C,N}$$

$$+\epsilon_{\mathrm{DSN,DIN}}\cdot D_{S,N}+\epsilon_{\mathrm{DSN,DIN}}\cdot D_{S,N}-U_{\mathrm{Cya}}\cdot P_{\mathrm{Cya}}-U_{\mathrm{UMD}}\cdot P_{\mathrm{UMD}}$$

$$-U_{\mathrm{Dtm}}\cdot P_{\mathrm{Dtm}}-U_{\mathrm{DDA}}\cdot P_{\mathrm{DDA}}-U_{\mathrm{Tri}}\cdot P_{\mathrm{Tri}} \tag{A11}$$

where:

$$U_{\mathrm{UMD}}(\mathrm{N,DIP},I)=\mu_{\mathrm{small}}\cdot\vartheta_{\mathrm{nif}}\cdot e^{-I/I_{\beta P}}\cdot\left(1-e^{-I/I_P}\right)\cdot\min\left(\frac{\mathrm{DIN}}{K_{S,N}+\mathrm{DIN}},\frac{\mathrm{DIP}}{K_{S,P}+\mathrm{DIP}}\right) \tag{A12}$$

$$U_{\mathrm{DDA}}(\mathrm{N,DIP},I)=\mu_{\mathrm{large}}\cdot\vartheta_{\mathrm{nif}}\cdot e^{-I/I_{\beta P}}\cdot\left(1-e^{-I/I_P}\right)$$

$$\cdot\min\left(\frac{\mathrm{DIN}}{K_{L,N}+\mathrm{DIN}},\frac{\mathrm{DIP}}{K_{L,P}+\mathrm{DIP}},\frac{\mathrm{Si}}{K_{\mathrm{Si}}+\mathrm{Si}}\right) \tag{A13}$$

$$U_{\mathrm{Tri}}(\mathrm{N,DIP},I)=\mu_{\mathrm{Tri}}\cdot\vartheta_{\mathrm{nif}}\cdot\left(1-e^{-I/I_P}\right)\cdot\min\left(\frac{\mathrm{DIN}}{K_{T,N}+\mathrm{DIN}},\frac{\mathrm{DIP}}{K_{T,P}+\mathrm{DIP}}\right) \tag{A14}$$

$$\frac{\mathrm{dSi}}{\mathrm{d}t}=\epsilon_{\mathrm{DCSi,Si}}\cdot D_{C,\mathrm{Si}}+\epsilon_{\mathrm{DSSi,Si}}\cdot D_{S,\mathrm{Si}}+\epsilon_{\mathrm{DLSi,Si}}\cdot D_{L,\mathrm{Si}}$$

$$-\alpha\frac{U_{\mathrm{Dtm}}}{R_{\mathrm{Si}}}\cdot P_{\mathrm{Dtm}}-\alpha\frac{G_{\mathrm{DDA}}}{R_{\mathrm{Si}}}\cdot P_{\mathrm{DDA}} \tag{A15}$$

BGD
10, 13931–13976, 2013

Acknowledgements. We would like to thank our many collaborators from the ANACONDAS project for their thoughtful contributions to this project. In particular, we would like to thank P. Yager, J. Goes, D. Steinberg, J. Montoya, and E. Carpenter for insightful conversations that informed the preparation of this manuscript. This work was supported by NSF Grant OCE-0933975.

References

Aumont, O., Maier-Reimer, E., Blain, S., and Monfray, P.: An ecosystem model of the global ocean including Fe, Si, P colimitations, Global Biogeochem. Cy., 17, 1060, doi:10.1029/2001gb001745, 2003.

Breitbarth, E., Oschlies, A., and LaRoche, J.: Physiological constraints on the global distribution of *Trichodesmium* – effect of temperature on diazotrophy, Biogeosciences, 4, 53–61, doi:10.5194/bg-4-53-2007, 2007.

Calbet, A.: Mesozooplankton grazing effect on primary production: a global comparative analysis in marine ecosystems, Limnol. Oceanogr., 46, 1824–1830, 2001.

Calbet, A. and Landry, M. R.: Phytoplankton growth, microzooplankton grazing, and carbon cycling in marine systems, Limnol. Oceanogr., 49, 51–57, 2004.

Calbet, A., Atienza, D., Henriksen, C. I., Saiz, E., and Adey, T. R.: Zooplankton grazing in the Atlantic Ocean: a latitudinal study, Deep-Sea Res. Pt. II, 56, 954–963, doi:10.1016/j.dsr2.2008.10.009, 2009.

Capone, D. G., Burns, J. A., Montoya, J. P., Subramaniam, A., Mahaffey, C., Gunderson, T., Michaels, A. F., and Carpenter, E. J.: Nitrogen fixation by *Trichodesmium* spp.: an important source of new nitrogen to the tropical and subtropical North Atlantic Ocean, Global Biogeochem. Cy., 19, GB2024, doi:10.1029/2004gb002331, 2005.

Carpenter, E. J., Montoya, J. P., Burns, J., Mulholland, M. R., Subramaniam, A., and Capone, D. G.: Extensive bloom of a N_2-fixing diatom/cyanobacterial association in the tropical Atlantic Ocean, Mar. Ecol.-Prog. Ser., 185, 273–283, 1999.

Coles, V. J. and Hood, R. R.: Modeling the impact of iron and phosphorus limitations on nitrogen fixation in the Atlantic Ocean, Biogeosciences, 4, 455–479, doi:10.5194/bg-4-455-2007, 2007.

BGD
10, 13931–13976, 2013

Coles, V. J., Brooks, M. T., Hopkins, J. H., Stukel, M. R., Yager, P. L., and Hood, R. R.: The pathways and properties of the Amazon River Plume in the tropical North Atlantic Ocean, J. Geophys. Res., in review, 2013.

Cooley, S. R. and Yager, P. L.: Physical and biological contributions to the western tropical North Atlantic Ocean carbon sink formed by the Amazon River plume, J. Geophys. Res.-Oceans, 111, C08018 doi:10.1029/2005jc002954, 2006.

Davenport, R., Neuer, S., Helmke, P., Perez-Marrero, J., and Llinas, O.: Primary productivity in the northern Canary Islands region as inferred from SeaWiFS imagery, Deep-Sea Res. Pt. II, 49, 3481–3496, doi:10.1016/s0967-0645(02)00095-4, 2002.

Dekaezemacker, J. and Bonnet, S.: Sensitivity of N_2 fixation to combined nitrogen forms (NO_3^- and NH_4^+) in two strains of the marine diazotroph *Crocosphaera watsonii* (Cyanobacteria), Mar. Ecol.-Prog. Ser., 438, 33–46, doi:10.3354/meps09297, 2011.

Falcon, L. I., Carpenter, E. J., Cipriano, F., Bergman, B., and Capone, D. G.: N_2 fixation by unicellular bacterioplankton from the Atlantic and Pacific oceans: phylogeny and in situ rates, Appl. Environ. Microb., 70, 765–770, doi:10.1128/aem.70.2.765-770.2004, 2004.

Fasham, M. J. R., Ducklow, H. W., and McKelvie, S. M.: A nitrogen-based model of plankton dynamics in the oceanic mixed layer, J. Mar. Res., 48, 591–639, 1990.

Fernández, A., Mouriño-Carballido, B., Bode, A., Varela, M., and Marañón, E.: Latitudinal distribution of *Trichodesmium* spp. and N_2 fixation in the Atlantic Ocean, Biogeosciences, 7, 3167–3176, doi:10.5194/bg-7-3167-2010, 2010.

Foster, R. A., Kuypers, M. M., Vagner, T., Paerl, R. W., Musat, N., and Zehr, J. P.: Nitrogen fixation and transfer in open ocean diatom-cyanobacterial symbioses, ISME J., 5, 1484–1493, 2011.

Halliwell, G. and Garraffo, Z.: Synthetic floats, drifters, and moorings in HYCOM, available at: http://hycom.org/attachments/067_float.pdf, last accessed: 18 April 2013, 2002.

Hood, R. R., Bates, N. R., Capone, D. G., and Olson, D. B.: Modeling the effect of nitrogen fixation on carbon and nitrogen fluxes at BATS, Deep-Sea Res. Pt. II, 48, 1609–1648, 2001.

Hood, R. R., Coles, V. J., and Capone, D. G.: Modeling the distribution of *Trichodesmium* and nitrogen fixation in the Atlantic Ocean, J. Geophys. Res.-Oceans, 109, C06006, doi:10.1029/2002jc001753, 2004.

Hu, C. M., Montgomery, E. T., Schmitt, R. W., and Muller-Karger, F. E.: The dispersal of the Amazon and Orinoco River water in the tropical Atlantic and Caribbean Sea:

BGD
10, 13931–13976, 2013

observation from space and S-PALACE floats, Deep-Sea Res. Pt. II, 51, 1151–1171, doi:10.1016/j.dsr2.2004.04.001, 2004.
Huskin, I., Anadon, R., Woodd-Walker, R. S., and Harris, R. P.: Basin-scale latitudinal patterns of copepod grazing in the Atlantic Ocean, J. Plankton Res., 23, 1361–1371, doi:10.1093/plankt/23.12.1361, 2001.
Isla, J. A., Llope, M., and Anadon, R.: Size-fractionated mesozooplankton biomass, metabolism and grazing along a 50° N–30° S transect of the Atlantic Ocean, J. Plankton Res., 26, 1301–1313, doi:10.1093/plankt/fbh121, 2004.
Lopez, E. and Anadon, R.: Copepod communities along an Atlantic Meridional Transect: abundance, size structure, and grazing rates, Deep-Sea Res. Pt. I, 55, 1375–1391, doi:10.1016/j.dsr.2008.05.012, 2008.
Luo, Y.-W., Doney, S. C., Anderson, L. A., Benavides, M., Berman-Frank, I., Bode, A., Bonnet, S., Boström, K. H., Böttjer, D., Capone, D. G., Carpenter, E. J., Chen, Y. L., Church, M. J., Dore, J. E., Falcón, L. I., Fernández, A., Foster, R. A., Furuya, K., Gómez, F., Gundersen, K., Hynes, A. M., Karl, D. M., Kitajima, S., Langlois, R. J., LaRoche, J., Letelier, R. M., Marañón, E., McGillicuddy Jr., D. J., Moisander, P. H., Moore, C. M., Mouriño-Carballido, B., Mulholland, M. R., Needoba, J. A., Orcutt, K. M., Poulton, A. J., Rahav, E., Raimbault, P., Rees, A. P., Riemann, L., Shiozaki, T., Subramaniam, A., Tyrrell, T., Turk-Kubo, K. A., Varela, M., Villareal, T. A., Webb, E. A., White, A. E., Wu, J., and Zehr, J. P.: Database of diazotrophs in global ocean: abundance, biomass and nitrogen fixation rates, Earth Syst. Sci. Data, 4, 47–73, doi:10.5194/essd-4-47-2012, 2012.
Maranon, E., Perez, V., Fernandez, E., Anadon, R., Bode, A., Gonzalez, N., Huskin, I., Isla, A., Moran, X. A. G., Mourino, B., Quevedo, M., Robinson, C., Serret, P., Teira, E., Varela, M. M., Woodward, E. M. S., and Zubkov, M. V.: Planktonic carbon budget in the eastern subtropical North Atlantic, Aquat. Microb. Ecol., 48, 261–275, 2007.
Monteiro, F. M., Follows, M. J., and Dutkiewicz, S.: Distribution of diverse nitrogen fixers in the global ocean, Global Biogeochem. Cy., 24, Gb3017, doi:10.1029/2009gb003731, 2010.
Montoya, J. P., Voss, M., and Capone, D. G.: Spatial variation in N_2-fixation rate and diazotroph activity in the Tropical Atlantic, Biogeosciences, 4, 369–376, doi:10.5194/bg-4-369-2007, 2007.
Moore, C. M., Mills, M. M., Achterberg, E. P., Geider, R. J., LaRoche, J., Lucas, M. I., McDonagh, E. L., Pan, X., Poulton, A. J., Rijkenberg, M. J. A., Suggett, D. J., Ussher, S. J., and

BGD
10, 13931–13976, 2013

Woodward, E. M. S.: Large-scale distribution of Atlantic nitrogen fixation controlled by iron availability, Nat. Geosci., 2, 867–871, doi:10.1038/ngeo667, 2009.
Moore, J. K., Doney, S. C., Kleypas, J. A., Glover, D. M., and Fung, I. Y.: An intermediate complexity marine ecosystem model for the global domain, Deep-Sea Res. Pt. II, 49, 403–462, 2002.
Moore, J. K., Doney, S. C., Lindsay, K., Mahowald, N., and Michaels, A. F.: Nitrogen fixation amplifies the ocean biogeochemical response to decadal timescale variations in mineral dust deposition, Tellus B, 58, 560–572, doi:10.1111/j.1600-0889.2006.00209.x, 2006.
Neuer, S., Freudenthal, T., Davenport, R., Llinas, O., and Rueda, M. J.: Seasonality of surface water properties and particle flux along a productivity gradient off NW Africa, Deep-Sea Res. Pt. II, 49, 3561–3576, 2002.
Perez, V., Fernandez, E., Maranon, E., Serret, P., Varela, R., Bode, A., Varela, M., Varela, M. M., Moran, X. A. G., Woodward, E. M. S., Kitidis, V., and Garcia-Soto, C.: Latitudinal distribution of microbial plankton abundance, production, and respiration in the Equatorial Atlantic in Autumn 2000, Deep-Sea Res. Pt. I, 52, 861–880, doi:10.1016/j.dsr.2005.01.002, 2005.
Perez, V., Fernandez, E., Maranon, E., Moran, X. A. G., and Zubkovc, M. V.: Vertical distribution of phytoplankton biomass, production and growth in the Atlantic subtropical gyres, Deep-Sea Res. Pt. I, 53, 1616–1634, doi:10.1016/j.dsr.2006.07.008, 2006.
Perry, G. D., Duffy, P. B., and Miller, N. L.: An extended data set of river discharges for validation of general circulation models, J. Geophys. Res.-Atmos., 101, 21339–21349, doi:10.1029/96jd00932, 1996.
Poulton, A. J., Holligan, P. M., Hickman, A., Kim, Y. N., Adey, T. R., Stinchcombe, M. C., Holeton, C., Root, S., and Woodward, E. M. S.: Phytoplankton carbon fixation, chlorophyll-biomass and diagnostic pigments in the Atlantic Ocean, Deep-Sea Res. Pt. II, 53, 1593–1610, doi:10.1016/j.dsr2.2006.05.007, 2006.
Quevedo, M. and Anadón, R.: Protist control of phytoplankton growth in the subtropical northeast Atlantic, Mar. Ecol.-Prog. Ser., 221, 29–38, 2001.
Rijkenberg, M. J. A., Langlois, R. J., Mills, M. M., Patey, M. D., Hill, P. G., Nielsdottir, M. C., Compton, T. J., LaRoche, J., and Achterberg, E. P.: Environmental forcing of nitrogen fixation in the eastern tropical and sub-tropical North Atlantic Ocean, PLoS One, 6, e28989, doi:10.1371/journal.pone.0028989, 2011.
Steele, M., Morley, R., and Ermold, W.: PHC: a global ocean hydrography with a high-quality arctic ocean, J. Climate, 14, 2079–2087, 2001.

BGD
10, 13931–13976, 2013

Stock, C. and Dunne, J.: Controls on the ratio of mesozooplankton production to primary production in marine ecosystems, Deep-Sea Res. Pt. I, 57, 95–112, doi:10.1016/j.dsr.2009.10.006, 2010.

Subramaniam, A., Yager, P. L., Carpenter, E. J., Mahaffey, C., Bjorkman, K., Cooley, S., Kustka, A. B., Montoya, J. P., Sanudo-Wilhelmy, S. A., Shipe, R., and Capone, D. G.: Amazon River enhances diazotrophy and carbon sequestration in the tropical North Atlantic Ocean, P. Natl. Acad. Sci. USA, 105, 10460–10465, doi:10.1073/pnas.0710279105, 2008.

Teira, E., Mourino, B., Maranon, E., Perez, V., Pazo, M. J., Serret, P., de Armas, D., Escanez, J., Woodward, E. M. S., and Fernandez, E.: Variability of chlorophyll and primary production in the Eastern North Atlantic Subtropical Gyre: potential factors affecting phytoplankton activity, Deep-Sea Res. Pt. I, 52, 569–588, doi:10.1016/j.dsr.2004.11.007, 2005.

Tilstone, G., Smyth, T., Poulton, A., and Hutson, R.: Measured and remotely sensed estimates of primary production in the Atlantic Ocean from 1998 to 2005, Deep-Sea Res. Pt. II, 56, 918–930, doi:10.1016/j.dsr2.2008.10.034, 2009.

Turk, K. A., Rees, A. P., Zehr, J. P., Pereira, N., Swift, P., Shelley, R., Lohan, M., Woodward, E. M. S., and Gilbert, J.: Nitrogen fixation and nitrogenase (nifH) expression in tropical waters of the eastern North Atlantic, ISME J., 5, 1201–1212, doi:10.1038/ismej.2010.205, 2011.

Villareal, T. A.: Laboratory culture and preliminary characterization of the nitrogen-fixing *Rhizosolenia–Richelia* symbiosis, Mar. Ecol., 11, 117–132, 1990.

Ye, Y., Volker, C., Bracher, A., Taylor, B., and Wolf-Gladrow, D. A.: Environmental controls on N_2 fixation by *Trichodesmium* in the tropical eastern North Atlantic Ocean – a model-based study, Deep-Sea Res. Pt. I, 64, 104–117, doi:10.1016/j.dsr.2012.01.004, 2012.

Yoshikawa, C., Coles, V. J., Hood, R. R., Capone, D. G., and Yoshida, N.: Modeling how surface nitrogen fixation influences subsurface nutrient patterns in the North Atlantic, J. Geophys. Res.-Oceans, 118, 2520–2534, 2013.

BGD
10, 13931–13976, 2013

Table A1. Parameter values.

Param	Description	Value	Units
α	fraction of uptake that goes to growth	0.7	
μ_{small}	max growth rate of cya	1.0	d^{-1}
μ_{large}	max growth rate of diatoms	3.0	d^{-1}
μ_{Tri}	max growth rate of Tricho	0.15	d^{-1}
ϑ_S	UMD diazo growth penalty	0.6	
ϑ_{NIF}	DDA growth penalty	0.67	
ϑ_S	DDA diazotrophic growth penalty	0.33	
$I_{\beta PS}$	Cya photoinhibition parameter	400	$W m^{-2}$
$I_{\beta PL}$	Dtm photoinhibition parameter	400	$W m^{-2}$
I_{PS}	Cya growth-irradiance parameter	20	$W m^{-2}$
I_{PL}	Dtm growth-irradiance parameter	40	$W m^{-2}$
I_{PT}	Tricho growth-irradiance parameter	70	$W m^{-2}$
$K_{S,N}$	Cya half-saturation for DIN	0.2	$\mu mol N L^{-1}$
$K_{L,N}$	Dtm half-saturation for DIN	1.2	$\mu mol N L^{-1}$
$K_{T,N}$	Tricho half-saturation for DIN	0.5	$\mu mol N L^{-1}$
$K_{S,P}$	Cya half-saturation for DIP	0.005	$\mu mol P L^{-1}$
$K_{L,P}$	Dtm half-saturation for DIP	0.01	$\mu mol P L^{-1}$
$K_{T,P}$	Tricho half-saturation for DIP	0.0077	$\mu mol P L^{-1}$
$K_{L,Si}$	Dtm half-saturation for Si	2.0	$\mu mol Si L^{-1}$
m_{PS}	Cya and UMD mortality	0.01	d^{-1}
m_{PL}	Dtm and DDAmortality	0.05	d^{-1}
m_{PT}	Tricho mortality	0.01	d^{-1}
m_{ZS}	Protozoan mortality	0.01	d^{-1}
m_{ZL}	Mesozooplankton mortality	0.01	d^{-1}
f	fraction of diatom mortality to D_S	0.25	d^{-1}
R_0	N : P ratio of non-diazotrophs	16	$mol mol^{-1}$
R_N	N : P ratio of diazotrophs	45	$mol mol^{-1}$
R_N	N : P ratio of diazotrophs	45	$mol mol^{-1}$
R_{Si}	N : Si ratio of diatoms	1.0	
G_{S0}	Protozoan max grazing rate	8.0	d^{-1}
G_{L0}	Mesozooplankton max grazing rate	2.0	d^{-1}
K_{ZS}	Protozoan half-saturation constant	2.7	$\mu mol N L^{-1}$
K_{ZL}	Mesozooplankton half-saturation constant	2.7	$\mu mol N L^{-1}$

BGD
10, 13931–13976, 2013

Table A1. Continued.

Param	Description	Value	Units
K_H	Higher Predator half-saturation constant	2.7	$\mu mol\,N\,L^{-1}$
γ_S	gross growth efficiency of protozoans	0.3	
γ_L	gross growth efficiency of mesozooplankton	0.3	
ε_S	egestion efficiency of protozoans	0.3	
ε_L	egestion efficiency of mesozooplankton	0.3	
ε_H	egestion efficiency of higher predators	0.43	
σ_S	Fraction of protozoan excretion to D_C	0.25	
σ_L	Fraction of mesozooplankton excretion to D_C	0.25	
σ_H	Fraction of higher predator excretion to D_C	0.25	
B_R	Basal metabolic rates of mesozooplankton	0.05	d^{-1}
π_{SS}	Protozoan preference for cya	1.0	
π_{SL}	Protozoan preference for Dtm	0.1	
π_{ST}	Protozoan preference for Tricho	0.01	
π_{SZ}	Protozoan preference for protozoans	0.1	
π_{SD}	Protozoan preference for large detritus	0.01	
π_{LL}	Mesozooplankton preference for Dtm	1.0	
π_{LT}	Mesozooplankton preference for Tricho	0.3	
π_{LZ}	Mesozooplankton preference for protozoans	0.3	
π_{LD}	Mesozooplankton preference for large detritus	0.3	
$\epsilon_{DCN,DIN}$	Remineralization rate of DCN	0.05	d^{-1}
$\epsilon_{DCP,DIP}$	Remineralization rate of DCP	0.25	d^{-1}
$\epsilon_{DCSi,Si}$	Remineralization rate of DCSi	0.8	d^{-1}
$\epsilon_{DSN,DIN}$	Remineralization rate of DSN	0.05	d^{-1}
$\epsilon_{DSP,DIP}$	Remineralization rate of DSP	0.25	d^{-1}
$\epsilon_{DSSi,Si}$	Remineralization rate of DSSi	0.8	d^{-1}
$\epsilon_{DLN,DIN}$	Remineralization rate of DLN	0.05	d^{-1}
$\epsilon_{DLP,DIP}$	Remineralization rate of DLP	0.25	d^{-1}
$\epsilon_{DLSi,Si}$	Remineralization rate of DLSi	0.8	d^{-1}
ω_S	Small detritus sinking rate	10	d^{-1}
ω_L	Large Detritus sinking rate	50	d^{-1}
Riv_{DIN}	DIN concentration in river	8.5	$\mu mol\,N\,L^{-1}$
Riv_{DIP}	DIP concentration in river	0.8	$\mu mol\,P\,L^{-1}$
Riv_{Si}	Si concentration in river	32.0	$\mu mol\,Si\,L^{-1}$

BGD
10, 13931–13976, 2013

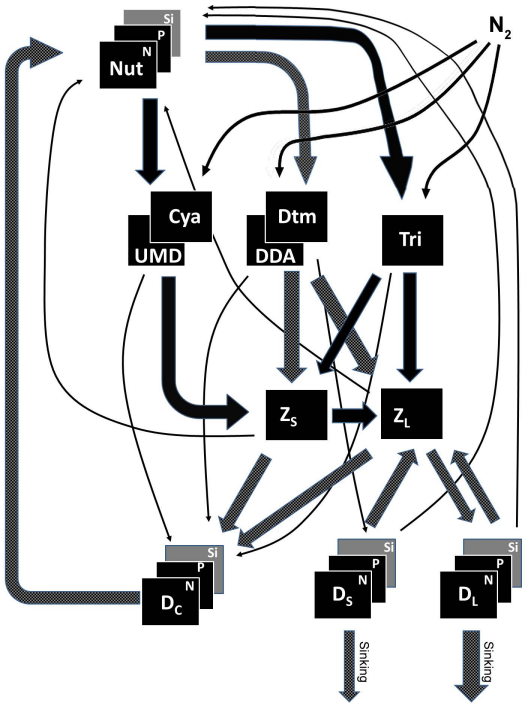

Fig. 1. Model description. Model contains 19 biological compartments: three nutrients (N, P, Si), five phytoplankton (cyanobacteria, Cya; unicellular microbial diazotrophs, UMD; diatoms, Dtm; diatom-diazotroph assemblages, DDA; and *Trichodesmium*, Tri), two zooplankton (Protozoans, Z_s; and mesozooplankton, Z_l), and three detrital size classes (dissolved and colloidal detritus, D_c; small detritus, D_s, and large detritus, D_l) each of which have three different element pools (N, P, Si) to allow variable stoichiometry of the detritus. Arrows depict model flows (transfer functions). Thin black arrows are minor flows. Solid black arrows are flows of only N and P. Hashed black arrows are flows of N, P, and Si.

BGD
10, 13931–13976, 2013

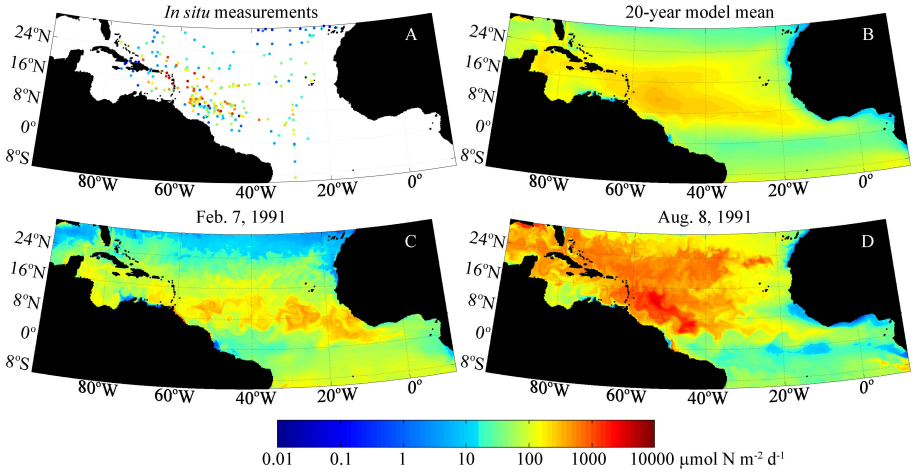

Fig. 2. Basin-scale nitrogen fixation. **(A)** shows in situ nitrogen fixation measurements compiled by Luo et al. (2012) on a logarithmic scale. **(B–D)** show model values representing the 20 yr model mean **(B)**, and single day values from 7 February 1991 **(C)** and 8 August 1991. These days were chosen because they showed the lowest and highest, respectively, rates of nitrogen fixation during the "normal" year of 1991 and hence highlight the seasonal variability in the model.

BGD
10, 13931–13976, 2013

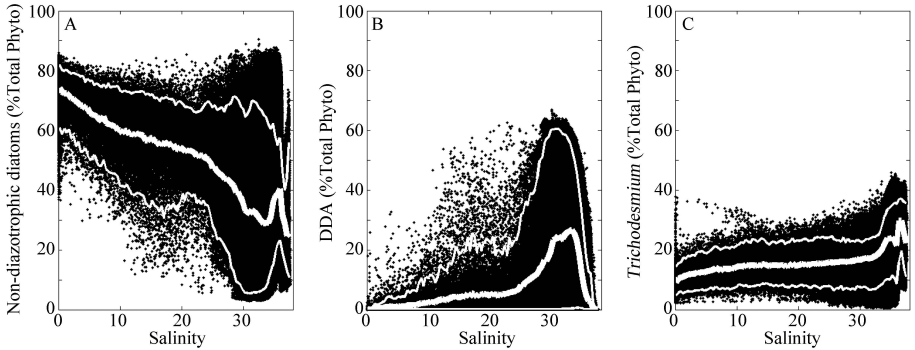

Fig. 3. Percentage contribution of phytoplankton taxa to total surface phytoplankton biomass along the salinity gradient in the ARP region. Coastal diatoms **(A)**, DDA **(B)**, *Trichodesmium* **(C)**. Thick white lines are the model means. Thin white lines are the 95 % confidence intervals.

BGD
10, 13931–13976, 2013

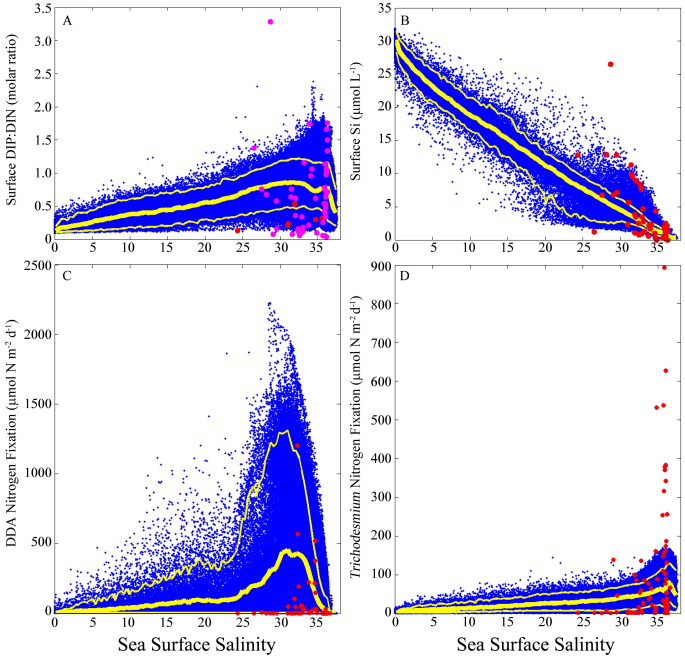

Fig. 4. Model-data property–salinity comparisons in the ARP. In all plots, blue points are model values, large red dots are in situ measurements from Subramaniam et al. (2008), thick yellow line is model mean, thin yellow lines are the 95 % confidence intervals. **(A)** shows surface nutrient P : N molar ratios. Magenta points are data points from Subramaniam et al. (2008) for which NO_3 was at or below their detection limit of 0.05 μM. **(B)** shows surface Si concentrations ($\mu mol\,L^{-1}$). **(C)** shows DDA nitrogen fixation ($\mu mol\,N\,m^{-2}\,d^{-1}$). **(D)** shows *Trichodesmium* nitrogen fixation ($\mu mol\,N\,m^{-2}\,d^{-1}$).

BGD
10, 13931–13976, 2013

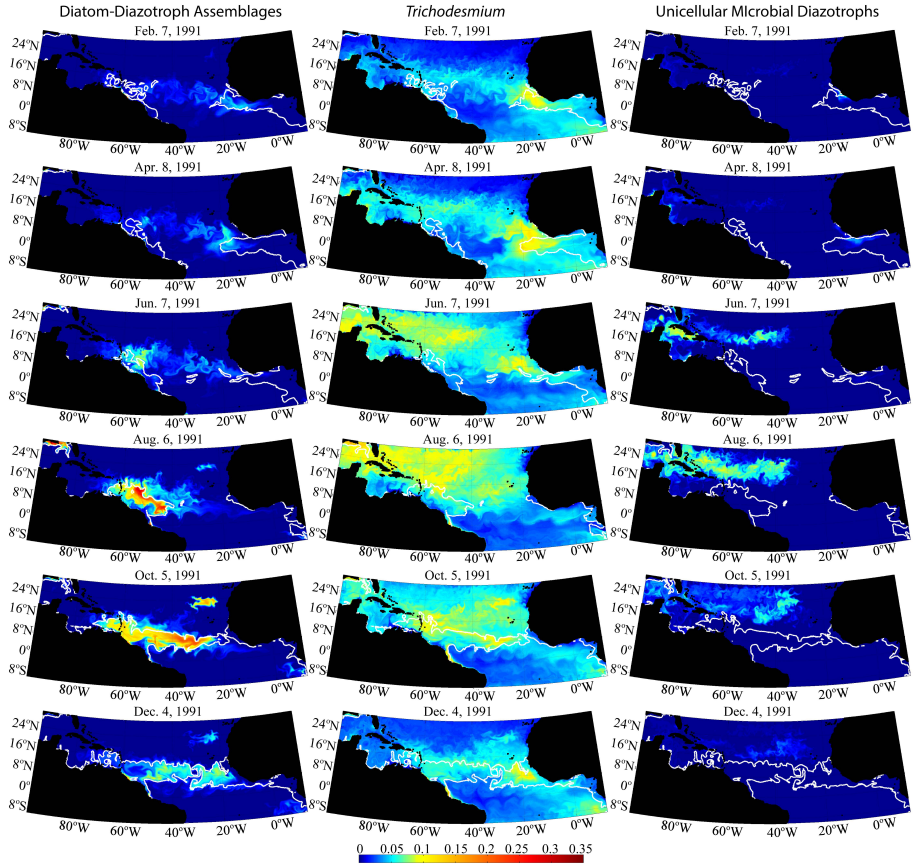

Fig. 5. Seasonal variability in model surface DDA (left), *Trichodesmium* (middle), and UMD (right) concentrations (μmol N L^{-1}). White lines show the 35 salinity contour.

BGD
10, 13931–13976, 2013

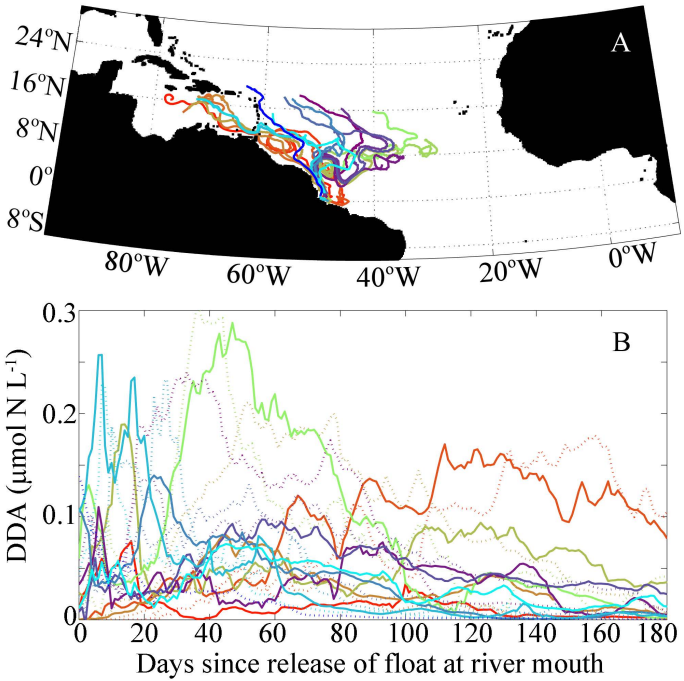

Fig. 6. Float trajectories for synthetic Lagrangian floats released at river mouth. **(A)** shows 20 randomly chosen float tracks (180 days shown for each float). **(B)** shows the concentration of DDA experienced by these 20 random floats. Colors match between panels. For ease of differentiating individual float tracks in **(B)**, half of the tracks are shown as dotted rather than solid lines.

BGD
10, 13931–13976, 2013

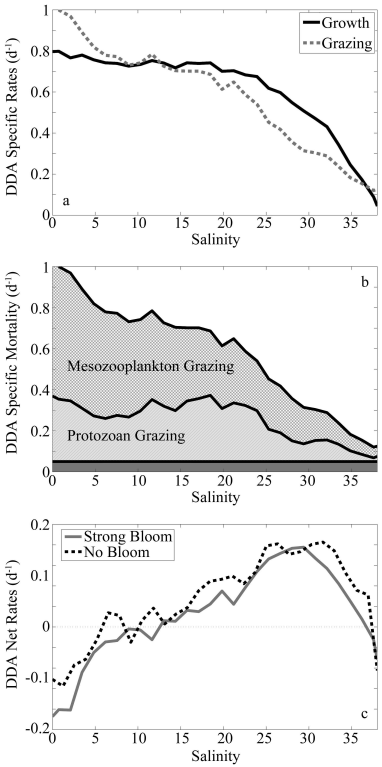

Fig. 7. DDA growth and grazing rates along synthetic Lagrangian float trajectories. **(a)** shows specific growth (solid black line) and mortality (gray dashed line) rates of DDA along strong bloom float trajectories (float trajectories with max DDA biomass > 0.2 µmol N L^{-1}) as a function of salinity. **(b)** subdivides the mortality rates from panel a into: natural or non-grazing mortality (solid gray bar at bottom), protozoan grazing (diagonal gray lines), and mesozooplankton grazing (gray checkerboard). **(c)** compares the net growth rates along strong bloom trajectories (solid gray line) to the growth rates along non-bloom trajectories (max DDA < 0.085 µmol N L^{-1}, dashed black line).

BGD
10, 13931–13976, 2013

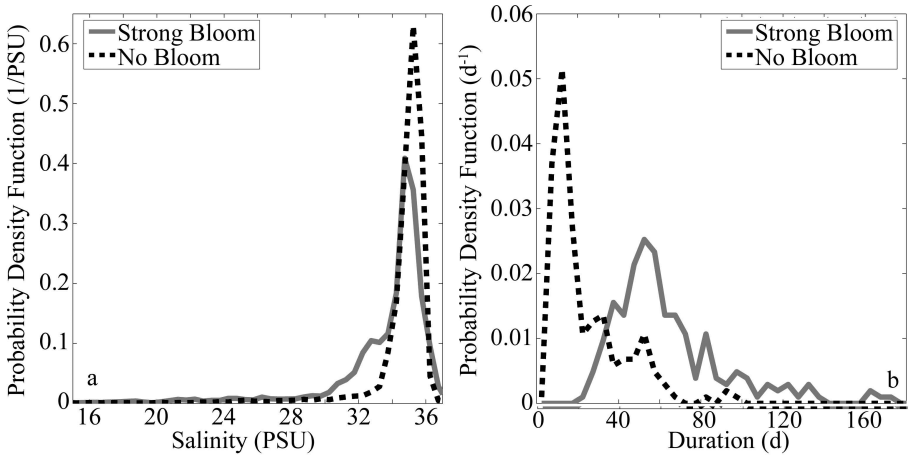

Fig. 8. Float salinity histograms. **(a)** shows the probability density function (PDF) of salinities experienced by synthetic Lagrangian floats in strong bloom floats (solid gray line) and non-bloom floats (dashed black line). **(b)** is the PDF of the duration of time that floats spend in the salinity range 20–34, which corresponds to the ideal growth conditions for DDA.

BGD
10, 13931–13976, 2013

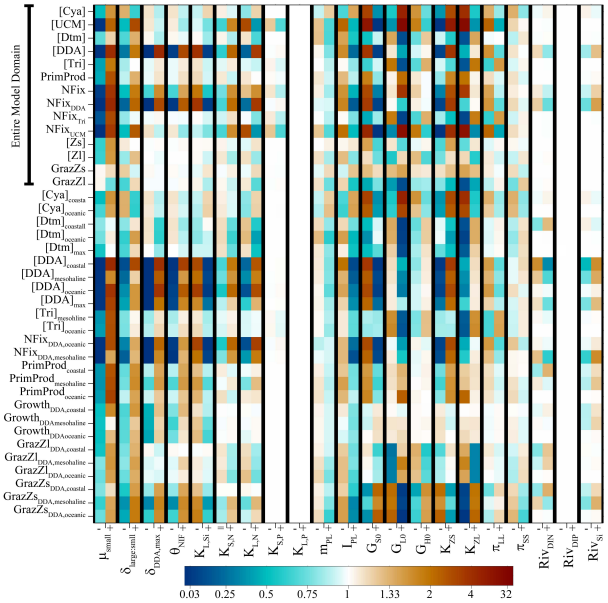

Fig. 9. Sensitivity Analysis. Relationship of important model outputs (rates and standing stocks, *y* axis) to variations in key model parameters (*x* axis). For each parameter, two four month simulations were conducted in which the parameter was either halved or doubled. Color axis shows the relationship of each model output at the end of the four month simulation to the equivalent model output in the base run. For instance, a result of 2 corresponds to a doubling of the model standing stock or rate. First 14 outputs are averaged over the entire basin. The rest are restricted to the ARP region. Parameters varied were: μ_{small} (which varies the growth rate of all phytoplankton proportionally, Eq. 19), $\delta_{large:small}$ (Eq. 19), $\delta_{DDA,max}$ (Eq. 20), θ_{NIF} (Eq. 21), $K_{L,Si}$ (Eqs. 6 and 8), $K_{S,N}$ (Eq. 2), $K_{L,N}$ (Eq. 6), $K_{S,P}$ (Eqs. 2 and 4), $K_{L,P}$ (Eqs. 6 and 8), m_{PL} (Eqs. 5 and 7), I_{PL} (Eqs. 6 and 8), G_{S0} (Eq. 13), G_{L0} (Eq. 17), G_{H0} (Eq. 15), K_{ZS} (Eq. 13), K_{ZL} (Eq. 17), π_{LL} (Eq. 18), π_{SS} (Eq. 14), Riv_{DIN}, Riv_{DIP}, Riv_{Si}.

BGD
10, 13931–13976, 2013

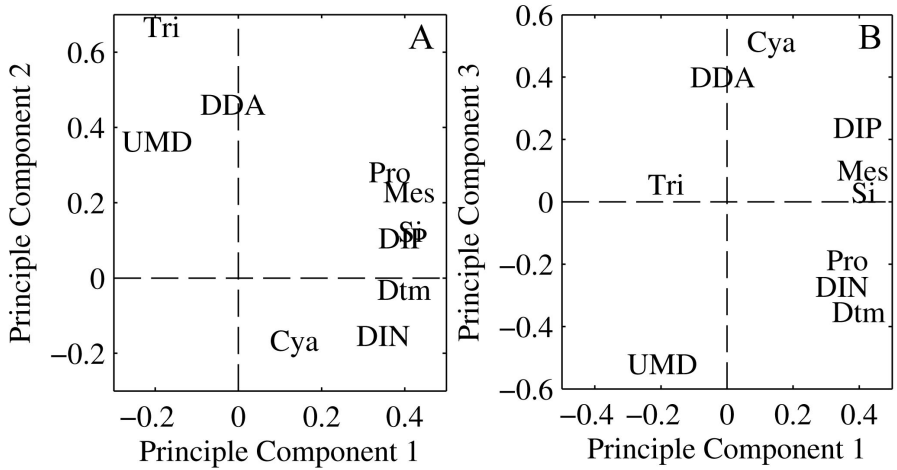

Fig. 10. Principle component (PC) analysis of model nutrients and living state variables. **(A)** shows PC 1 (39.5 % of the variance) on the *x* axis and PC 2 (15.8 % of the variance) on the *y* axis. **(B)** again has PC 1 on the *x* axis, but has PC 3 (12.7 % of the variance) on the *y* axis.

BGD
10, 13931–13976, 2013

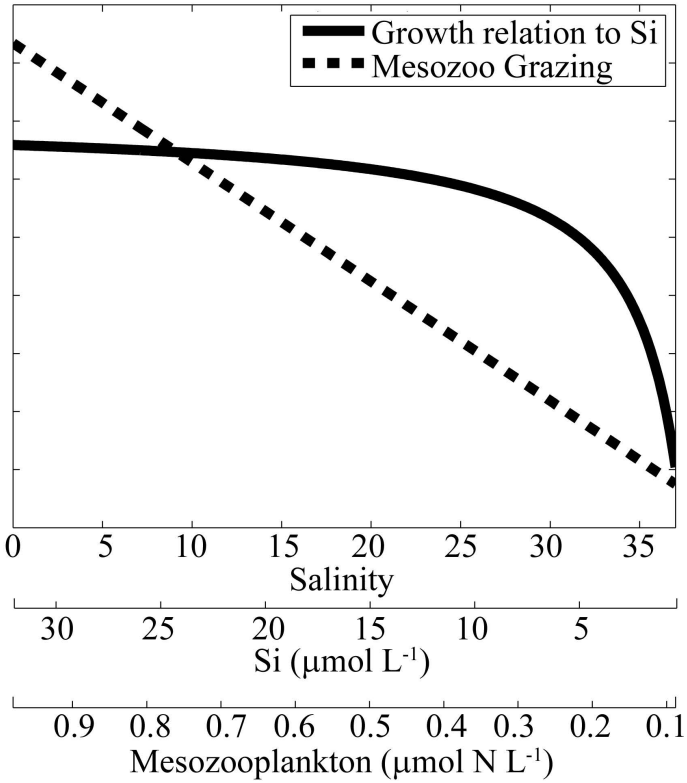

Fig. 11. Conceptual diagram of the relationship of DDA growth and loss rates to conservative mixing losses of Si and mesozooplankton along the salinity gradient. Note that we have put no values on the *y* axis since actual grazing rates will be dependent on the concentrations of all phytoplankton taxa and growth rates are dependent on light, both of which vary along the salinity gradient. Plot is only intended to show the different shape of DDA net growth rate responses to conservative mixing losses of nutrients and grazers.

BGD
10, 13931–13976, 2013